Synthesis of Oxide-Based Composite Solid Electrolyte for Lithium Batteries

By

HAFIZ MUHAMMAD HASEEB

Reg. No. 00000320053

Session 2019-21

Supervised by

Dr. Ghulam Ali

US-Pakistan Center for Advanced Studies in Energy (USPCAS-E)

National University of Sciences and Technology (NUST)

H-12, Islamabad 44000, Pakistan

September 2022

Synthesis of Oxide-Based Composite Solid Electrolyte for Lithium Batteries

By

HAFIZ MUHAMMAD HASEEB

Reg. No. 00000320053

Session 2019-21

Supervised by

Dr. Ghulam Ali

A Thesis Submitted to the US-Pakistan Center for Advanced Studies in Energy in partial fulfillment of the requirements for the degree of MASTER of SCIENCE in

Energy Systems Engineering

US-Pakistan Center for Advanced Studies in Energy (USPCAS-E)

National University of Sciences and Technology (NUST)

H-12, Islamabad 44000, Pakistan

September 2022

THESIS ACCEPTANCE CERTIFICATE

Certified that final copy of MS/MPhil thesis written by **Mr. HAFIZ MUHAMMAD HASEEB** (Registration No. 00000320053), of US-Pakistan Center for Advanced Studies in Energy (USPCAS-E) has been vetted by undersigned, found complete in all respects as per NUST Statues/Regulations, is within the similarity indices limit and is accepted as partial fulfillment for the award of MS degree. It is further certified that necessary amendments as pointed out by GEC members of the scholar have also been incorporated in the said thesis.

Signature: _____

Name of Supervisor: _____

Date: _____

Signature (HoD): _____

Date: _____

Signature (Dean/Principal): _____

Date: _____

Certificate

This is to certify that work in this thesis has been carried out by **Mr. HAFIZ MUHAMMAD HASEEB** and completed under my supervision in Synthesis and Energy Storage laboratory, US-Pakistan Center for Advanced Studies in Energy (USPCAS-E), National University of Sciences and Technology, H-12, Islamabad, Pakistan.

Supervisor: _____

Dr. Ghulam Ali
USPCAS-E
NUST, Islamabad

GEC member 1: _____

Prof. Dr. Naseem Iqbal
USPCAS-E
NUST, Islamabad

GEC member 2: _____

Dr. Sehar Shakir
USPCAS-E
NUST, Islamabad

GEC member 3: _____

Dr. Mustafa Anwar
USPCAS-E
NUST, Islamabad

HOD-ESE: _____

Dr. Rabia Liaquat
USPCAS-E
NUST, Islamabad

Dean/Principal: _____

Prof. Dr. Adeel Waqas
USPCAS-E
NUST, Islamabad

Dedication

To my parents, who supported me in every aspect of life and my siblings.

Acknowledgments

First and foremost, I am thankful to Almighty ALLAH who is the creator and author of knowledge. Indeed, without YOUR blessings, this mammoth task would not have been possible. And I acknowledge that without YOUR willingness and guidance, I would not have done a single task. I am grateful to my parents for their unconditional love and sacrifices. I am forever in your debt for your encouragement, financial and moral support. Thank you for keeping confidence in me.

I would like to express my sincere gratitude to my research supervisor, Dr. Ghulam Ali for letting me be part of the research group at Advanced Energy Materials Lab, USPCAS-E, NUST, Islamabad. I feel privileged to have worked under his kind supervision. It's the blend of his patience, persistence, guidance, and motivation that made me accomplish my research aims in due time. He polished my research skills and I have learned a lot under his supervision and guidance.

I would like to thank my GEC members Dr. Naseem Iqbal, Dr. Mustafa Anwar, and Dr. Sehar Shakir for their guidance and help throughout my research. I profusely thank my brother Altamash Shabbir for his immense support, always being there for me whenever I needed help. I am also thankful to the staff of Synthesis and Energy Storage Lab specially Engineer Naveed, and Advanced energy materials lab engineer Mr. Asghar Ali who helped in my research and gave valuable advice during my experimentation. . Also, all my friends for their support both academically and in general. And to life, an extraordinary experience with so many things to enjoy within a short span. Thank you for giving me so much in the years past, and for more to discover in the years to come.

Abstract

One of the most electrifying and interesting supporting components for the advancement of next-generation lithium batteries is a solid-state electrolyte. Oxide-based solid electrolytes are gaining popularity among researchers owing to their great stability, although they have inadequate ionic conductivity due to high grain boundary resistance. In this work, a novel oxide-based ternary composite ($AlPO_4$-SiO_2-$Li_4P_2O_7$) electrolyte is synthesized via a conventional solid-state process with excellent water stability and high ionic conductivity. The crystallographic structure of ternary composite is confirmed using X-ray diffraction and has a significant effect on ionic conductivity. The thermogravimetric analysis result shows a 22.26 wt.% loss in the region of 25 °C to 900 °C due to the degradation of volatile constituents including nitrates, chlorides, and water. BET results revealed that the material is compact and dense and having low porosity and surface area. The morphological assessment is carried out using scanning electron microscopy to observe the growth of grains. The Raman and Fourier transformed infra-red spectroscopies are used to scrutinize the structural and functional group analysis of the solid-state electrolyte. Electrochemical impedance spectroscopy is used to evaluate ionic conductivities. The ternary composite sintered at 900 °C has shown ionic conductivity of 2.21×10^{-4} S cm^{-1} at ambient temperature. These findings suggest that a solid electrolyte composed of ternary composites could be a credible candidate for lithium batteries.

Keywords: Lithium batteries; solid-state electrolyte; ternary composite; dopants; ionic conductivity

Table of Contents

List of Figures

List of Tables

List of Abbreviations

LIBs	Lithium-ion batteries
TR	Thermal runaway
SSEs	Solid state electrolyte
EV	Electric vehicle
HEV	Hybrid electric vehicle
Li	Lithium
ASSLBs	All solid-state lithium-ion batteries
MOF	Metal organic framework
NASICON	Sodium superionic conductor
LISICON	Lithium superionic conductor
Li-ion	Lithium ion
Mn	Manganese
Si	Silicon
XRD	X ray Diffraction
Co	Cobalt
SEM	Scanning Electron Microscopy
EIS	Electrochemical impedance spectroscopy
σ	Ionic conductivity
FTIR	Fourier transform infrared spectroscopy
EDS	Energy dispersive X-ray spectroscopy
V	Voltage

Chapter 1: Introduction

1.1 Background

Non-renewable energy sources include coal, oil, and natural gas, while renewable energy sources include the sun, water, biomass and wind. The transportation, manufacturing, and power generation sectors made good use of conventional, or nonrenewable, energy sources during the twentieth century. The depletion of fossil fuels and the environmental hazards posed by conventional energy sources have pushed renewable energy sources to the forefront in the last decade [1]. A major drawback to replacing conventional energy systems with renewable energy systems is the lack of reliability of renewable sources of energy, which are both environmentally friendly and sustainable.

These energy systems can be more reliable if they are paired with storage devices. When used in electric vehicles (EVs), batteries have the potential to revolutionize transportation by serving as an alternative to gasoline and diesel-powered vehicles [2]. To achieve a clean energy future, the importance of technology in renewable energy and electric storage cannot be overstated. Electricity storage is listed as one of the most critical uncertainties by World Issues Monitor 2017. Improvements in electrical storage technology have the potential to be a game changer in the fight against the main issues surrounding energy efficiency.

Electrochemical secondary batteries are still the primary method of storing electricity. Based on energy density, different storage mediums are compared to each other. Electrochemical processes can only be used in portable devices if they have a high energy density per unit weight [2]. Certain breakthroughs in nickel hydride and lithium ion battery technology have made their way into the mobile and transportation markets [3], including laptops, tools; cameras; mobile phones; electric vehicles; and hybrid electric vehicles [4]. LIBs, as well as other battery systems like lithium air, lithium Sulphur, and redox flow batteries, are the focus of intense research [5]. As with conventional batteries, redox reactions take place at the electrode-electrolyte interface while ions diffuse through the

electrolyte. The main difference between LIBs and conventional batteries is the solid-state mass diffusion [6].

1.2 Development of lithium ion batteries

The LIB's ESS market is expected to grow at a steady pace, according to the Panasonic Group (Sanyo). Assumption that the current battery purchase trend will continue, based on market research and projected future Li-ion battery prices [7]. The use of LIBs instead of lead acid batteries for energy storage and distribution and transmission, as well as investment substitution, are all viable options for the general public. For the purposes of this discussion, we assume that lithium is not used for energy storage. With these points in mind, LIBs have shown great progress in residential areas since 2017 [8].

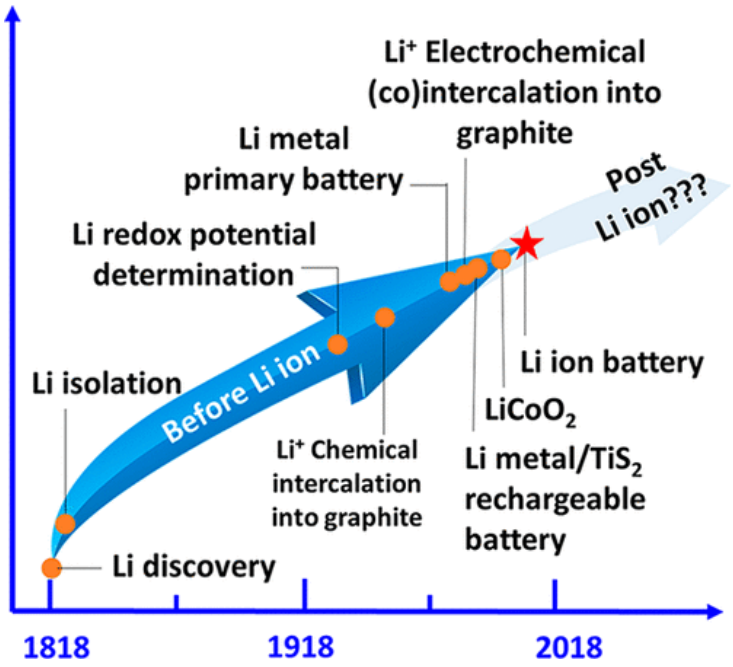

Figure 1-1. Roadmap for next generation Li-ion battery development [9].

In LIBs, the positive and negative electrode materials are lithium intercalation compounds. As the battery is charged and discharged, the lithium ions intercalate and deintercalated from the electrodes. Lithium-ion batteries are sometimes referred to as "rocking chair batteries" because of the movement of lithium ion between the positive and negative electrodes. Lithium cobalt oxide ($LiCoO_2$) batteries were first made

commercially available by Sony Co., Japan over two decades ago [10]. $LiCoO_2$ was used as the cathode, Graphite (C) was used as the negative electrode, and a non-aqueous electrolyte was used for the conduction of Li^+ in this battery design. High energy density LIBs have recently been the focus of increased research into electrode and electrolyte materials [11].

The Authority of UK Atomic energy published a patent showing that the insertion and deintercalation of Ax is reversible in the material with the structural formula $A_xM_yO_2$ insertion and deintercalation of A_x is reversible. When SONY used this patent in 1990, they used a $LiCoO_2$/soft carbon chemistry [12]. A camcorder TR-1 application sparked the first mass production of $LiCoO_2$/hard carbon [13].

1.3 Operating principle of lithium ion batteries

Anode material is intercalated with Li^+ ions, which are released from the host matrix of the cathode and travel through the outer circuit during charging.

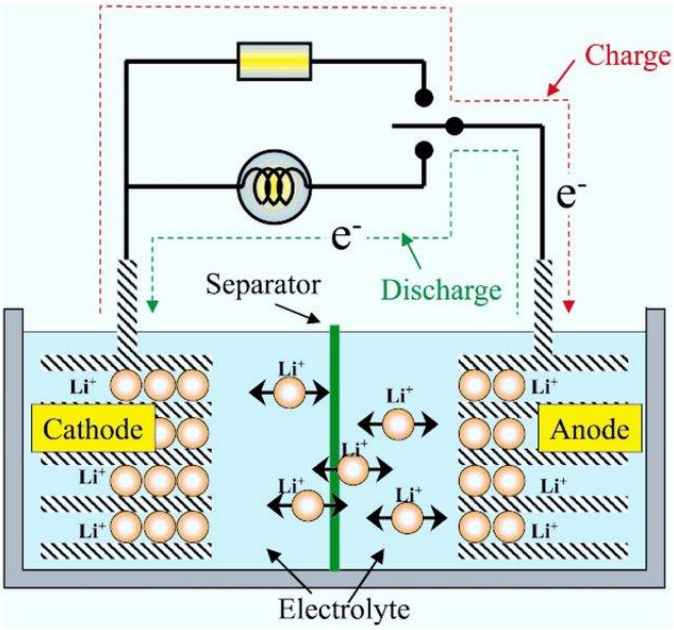

Figure 1-2. Li-ion battery operating principle [14].

Anode to cathode electrochemical reduction occurs when lithium ions are intercalated into a host material in the reverse mechanism of discharge, i.e. electrons travel through the outer circuit and power various systems from the anode to cathode. The cathode and anode

of the battery undergo an insertion reaction in the electrochemistry of the battery. The anode and cathode materials that participate in the insertion and extraction processes have layered or tunnel structures that establish an insertion mechanism involving the movement of Li^+ cations. Graphitic carbon cathodes have replaced lithium metal anodes as the primary source of lithium. When lithium metal oxides of the form $LiMO_2$ (where M denotes a transition metal) and graphite are used as an anode, the half reaction is given by:

In this case, the cathode side:

$$LiMO_2 \leftrightarrow Li_{1-x}MO_2 + xLi^+ + xe^-$$

In this case, the anode:

$$xLi^+ + xe^- + 6C \leftrightarrow Li_xC_6$$

Charge causes the transition metal oxide to go from M^{+3} to M^{+4}, while discharge reduces it from M^{+4} to M^{+3}, reversing the process.

1.4 Contribution of lithium ion batteries in power sector

The LIB technology and industry has dominated the power supply for cell phones, computers and digital cameras, as well as numerous military/renewable applications. Furthermore, the use of LIB in HEVs raises concerns about the safety of large-scale batteries. Secondary lithium battery systems are hindering this industry's growth because of their high-cost components and materials.

Electrical storage technological improvements can play dynamic role to stamp out the main concerns affiliated with energy efficiency. Electric storage is still chiefly based on electrochemical secondary batteries. For storing energy, the evaluation of different storage mediums is done based on energy density. Energy per unit weight of electrochemical process dictates its applicability in portable devices. Nickel hydride and Li ion batteries (LIBs) have made certain breakthroughs and have penetrated the mobile and transport markets such as laptops, tools, cameras, mobile phones, EVs, Hybrid electric vehicles (HEVs) etc. Secure growth is estimated by Panasonic Group (Sanyo) for ESS market potential of the LIB. Simulation assuming continuation of purchase trend of battery keeping in view market survey and Li ion future price. Community use for energy storage

and investment substitution for distribution and transmission and the use of LIBs instead of lead acid battery considering its safe maintenance in power sector. Further assuming no lithium use concerning to energy storage. Keeping all these points in consideration indicates the progressiveness of LIBs especially in residential areas starting from 2017.

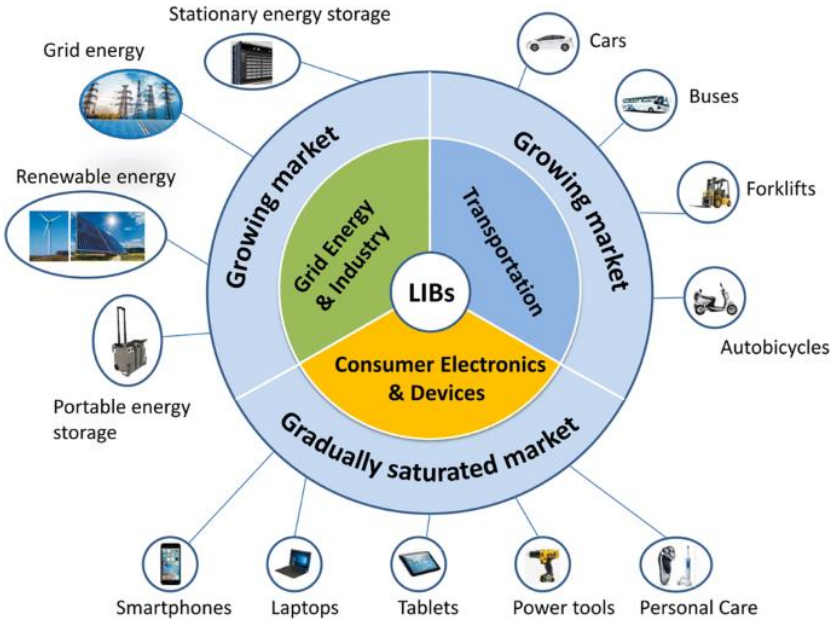

Figure 1-3. Power applications of lithium ion batteries [15].

1.5 Safety concerns about lithium ion batteries

Battery elements (cathode, anode, electrolyte, separators, and current collectors) and the battery system as a whole fail during abuse conditions [16], which is the primary cause of safety issues in LIBs. Overcharging, corrosion of the current collectors, and gas evolution are just a few of the symptoms of a failing battery system [17].

1.5.1 Evolution of the use of gas

The electrolyte in LIBs reacts with electrode materials at the electrode/electrolyte interface at high voltage levels 4V. Interfacial reactions between the cathode material and the organic solvents in the electrolyte cause gas evolution in LIBs. These are the conditions in which LIBs produce gas:

- A normal typical cycling
- Overcharge

- Temperatures in excess of 100 ℉
- The initial charge process

Carbon monoxide CO, hydrogen H_2, and ethylene C_2H_4 are the main first reaction gases that are generated during the first charge process. Carbon dioxide CO_2, carbon monoxide CO, ethylene C_2H_4, methane CH_4, and ethane C_2H_6 are all released during regular cycling at the required voltage. During the oxidation and reduction of the electrolyte at the electrode surface, these gases are produced. Carbon dioxide is produced by the oxidation reaction, whereas the reduction reaction is responsible for the production of the other gases [18].

More oxidation and reduction reactions occur during overcharging than in cycling conditions. There is a small amount of hydrocarbons in H_2 gas generated at both the cathode and anode surfaces. However, the amount of gas released is higher than in normal operating conditions [19]. As with the release of CO_2 from the cathode surface, there is also carbon monoxide CO from both electrode surfaces when storage is performed at high temperatures.

1.5.2 Formation of Dendritic Rods

The formation of lithium dendrites on the anode of LIBs is a major contributor to internal short circuits. Branches of dendrites penetrate the polymer separator, causing an internal short circuit. Li dendrites have been the subject of numerous investigations into their behaviour [20]. Higher current densities and the incorporation of Li foil were found to support the growth of Li dendrites. After 38 hours of continuous voltage discharge, dendrites begin to form, and after 100 hours, a single dendrite reaches the positive electrode and creates an internal short circuit [21].

The overcharge conditions are associated with high rated oxidation and reduction reactions than normal cycling conditions. At cathode the O_2 gas is generated and at anode surface the H_2 gas is generated which contains small quantity of hydrocarbons. The gases released are the same as in normal operating conditions however, the amount of gas release is higher [22]. Similarly, the gases released during storage under high temperatures include carbon dioxide CO_2 at cathode surface and carbon monoxide CO at both electrode surfaces.

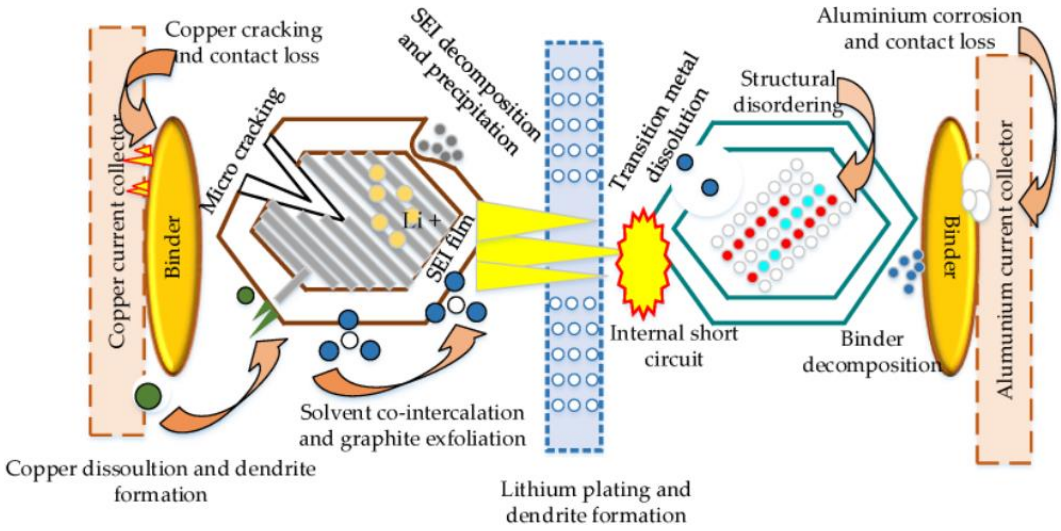

Figure 1-4. Degradation mechanism of Li-ion batteries [23].

1.5.3 Thermal runaway

Thermal runaway is a term used to describe the rise in temperature that occurs as a result of the abuse conditions. In the following section, we'll go over thermal runaway in more detail.

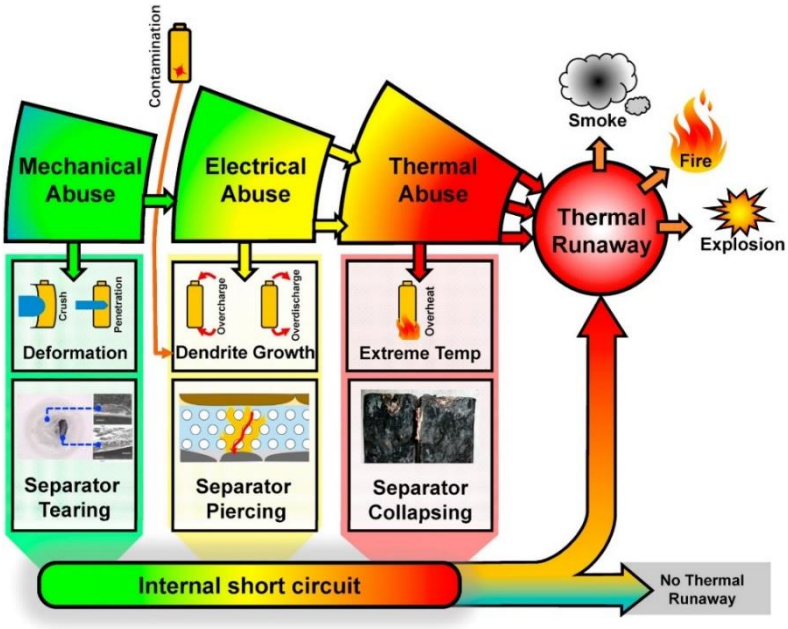

Figure 1-5. Thermal runaway mechanism of Li-ion batteries [24].

1.5.4 Dissolution of current collectors

In LIBs, the dissolution of current collectors such as aluminum metal Al and copper foil Cu is caused by overcharging and undercharging [25]. The short circuit in a LIB is caused by the presence of a conductive metal, which connects the positive and negative electrodes, resulting in a huge current and a rise in temperature and heat generation. After corrosion, the conductive metals Al and Cu can cause a battery short circuit [26]. An over discharge of the battery causes the dissolution of copper (Cu). The dissolution of Cu occurs at the anode surface at high potential values because of over discharge [27].

The positive electrode's current collector is made of Al, which is stable in both air and water. The passivation of the AlF_3 layer on the Al_2O_3 layer of the Al collector results in the dissolution of Al. Because of this dissolution, Al dendrites form on the anode surface, and the corroding current collectors of the electrodes support the diffusion of Al fragments into the electrolyte [28]. Corrosion on a large scale can cause the entire battery to fail due to the cracking and degradation of the cathode material [29].

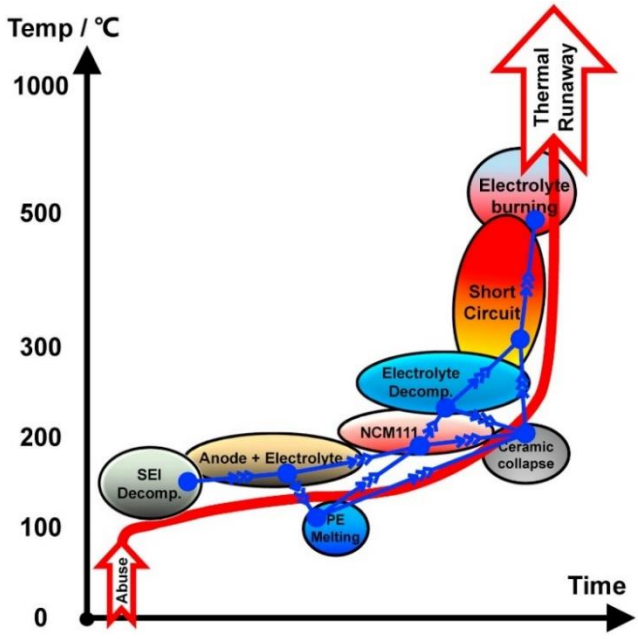

Figure 1-6. Thermal degradation of Li-ion batteries for EVs [30].

1.6 Components of lithium ion batteries

1.6.1 Materials for cathode

It is possible to alter cathode materials by coating them or substituting elements. Thermal stability can be improved by applying a surface coating [30]. Surface coating of was applied to the cathode material to conduct an experiment. The temperature of the exothermic reaction was delayed by 9℃ [31]. Progress in cathode material surface coating has recently been reviewed, the replacement of elements in the cathode can also improve the cathode's properties. The cathode material they created using the combustion method had the highest initial capacity of 138.6 mAh g^{-1} with better cycling stability [32].

1.6.2 Components for anode

The thermal conductivity and capacity of anodes can be improved further by applying a surface coating to the metal. The development of new materials that are both safe and more effective is being researched. Solid-electrolyte interface layer (SEI) stability is critical for an anode [33]. On graphite anodes, SEI formation is influenced by the electrolyte composition and the temperatures of thermal reactions taking place at the anode [34].

1.6.3 Electrolyte for lithium ion batteries

In 2000, D. D. MacNeil et al. discussed the importance of electrolyte to LIB safety. Because they are flammable, electrolytes such as organic carbonate solvents put LIBs at risk for explosion. Lithiated graphite and delithiated cathodes react strongly to alkyl based solvents at elevated temperatures [35]. The use of additives to improve carbonate-based electrolytes can lessen their dangers. It's also possible to reduce the risk of flammability by developing nonflammable solid state electrolytes, polymers, and room temperature molecular salts (such as Ionic Liquids).

Analysis of the behaviour of liquid electrolyte in and the development of a new electrolyte salt with better performance than has been done by M. Schmidt and colleagues. Thermally unstable and decomposes to and, the electrolyte used in lithium-ion cells is the subject of this study. Degrading the cell performance, the hydrolysis produces HF. New electrolyte salts, known as lithium fluoroalkyl phosphates, were introduced to overcome hydrolysis. In terms of hydrolysis resistance and conductivity, the resulting salt is on a par with [36].

Ionic liquids at room temperature are non-flammable and low-volatile, according to J.-H. Shin and coworkers. The low conductivity of ionic liquids is a major drawback. Lithium ions flow more freely through ionic liquids than through polymer-based electrolytes, but ionic liquids are less stable in a lithium-ion battery environment [37].

1.7 Battery management system

In the event that the battery's safe limits have been exceeded, the BMS protects it. Among other things, the battery management system (BMS) ensures that the battery operates within a specific voltage and temperature range, as well as provides protection from overheating, overcharging, and overcharging [38]. Because the performance of lithium-ion batteries is greatly affected by ambient temperature, it is necessary to have an effective battery management system in place [39].

An advanced BMS's fault diagnosis function is critical to its overall safety [40]. The detection of ISC, on the other hand, is a difficult model-based diagnostic task. In order to detect ISC, many algorithms have been developed, but they are ineffective; these algorithms should be more accurate, sensitive, and quick [41].

According to Mohammadian et al., BMS can also be divided into internal and external thermal management (ITM and ETM) (ETM) [42]. To prevent battery cell overheating, an ITM system, also known as intrinsic safety management, should dissipate heat. Electrolyte flows through the micro-channels of electrodes as a coolant, according to the author's proposal [43]. Because of its low cooling efficiency and difficult implementation, the ITM method is ineffective in real-world applications [44].

An 8-C battery pack was used to test Zheng et al claim that an ETM system improves heat dissipation from the external environment by using air cooling, phase change materials (PCM) cooling, and a combined liquid cooling and PCM cooling model [45]. The system showed improved results as it controlled the temperature well. Once an issue occurs, countermeasures like warning and fire extinguishers need to be taken, such as the BMS and intrinsic safety measures [46-49].

1.8 Problem statement

Lithium ion batteries are fire sensitive as the liquid electrolyte used in the Li-ion batteries are flammables. Replacing the flammable liquid electrolyte with a solid one would be

desirable. During the migration of Li-ions high grain boundary resistances faced by ions due to this the grain boundary resistance of solid state electrolytes for Li-ion batteries is high and low grain boundary conductivity.

1.9 Objectives

- To synthesize the metal doped composite solid state electrolyte for safer LIBs.
- To synthesize economical material for solid electrolyte using low cost precursors.
- Structural and morphological Characterization of synthesized material.
- To improve the ionic conductivity.

1.10 Scope of work

- Higher energy density batteries with improved ionic conductivity.
- Make the Li-ion batteries reliable and safe.
- Simple packaging requirements and better charging cycle.

Summary

In this chapter, we have learned about the lithium ion batteries as an energy storage device, as well as the potential hazards that can arise when it's put to use in high-density settings. Details about problems related to Li-ion batteries and possible mitigation methods are provided. A detailed discussion of solid electrolytes and their performance parameters is provided in the following chapter.

References

[1] P. Moriarty and D. Honnery, "What is the global potential for renewable energy?," *Renew. Sustain. Energy Rev.*, vol. 16, no. 1, pp. 244–252, 2012, doi: 10.1016/j.rser.2011.07.151.

[2] B. Diouf and R. Pode, "Potential of lithium-ion batteries in renewable energy," *Renew. Energy*, vol. 76, pp. 375–380, 2015, doi: 10.1016/j.renene.2014.11.058.

[3] F. Jia, K. Soucie, S. Alisat, D. Curtin, and M. Pratt, "Are environmental issues moral issues? Moral identity in relation to protecting the natural world," *J. Environ. Psychol.*, vol. 52, pp. 104–113, 2017, doi: 10.1016/j.jenvp.2017.06.004.

[4] X. Tang, W. Yang, X. Hu, and D. Zhang, "A novel simplified model for torsional vibration analysis of a series-parallel hybrid electric vehicle," *Mech. Syst. Signal Process.*, vol. 85, pp. 329–338, 2017, doi: 10.1016/j.ymssp.2016.08.020.

[5] T. H. Kim, J. S. Park, S. K. Chang, S. Choi, J. H. Ryu, and H. K. Song, "The current move of lithium ion batteries towards the next phase," *Adv. Energy Mater.*, vol. 2, no. 7, pp. 860–872, 2012, doi: 10.1002/aenm.201200028.

[6] Y. Sun, "Lithium ion conducting membranes for lithium-air batteries," *Nano Energy*, vol. 2, no. 5, pp. 801–816, 2013, doi: 10.1016/j.nanoen.2013.02.003.

[7] J. Scheers, S. Fantini, and P. Johansson, "A review of electrolytes for lithium-sulphur batteries," *J. Power Sources*, vol. 255, pp. 204–218, 2014, doi: 10.1016/j.jpowsour.2014.01.023.

[8] T. Kojima, T. Ishizu, T. Horiba, and M. Yoshikawa, "Development of lithium-ion battery for fuel cell hybrid electric vehicle application," *J. Power Sources*, vol. 189, no. 1, pp. 859–863, 2009, doi: 10.1016/j.jpowsour.2008.10.082.

[9] G. E. Blomgren, "The Development and Future of Lithium Ion Batteries," *J. Electrochem. Soc.*, vol. 164, no. 1, pp. A5019–A5025, 2017, doi: 10.1149/2.0251701jes.

[10] M. Armand *et al.*, "Lithium-ion batteries – Current state of the art and anticipated developments," *J. Power Sources*, vol. 479, no. June, 2020, doi:

10.1016/j.jpowsour.2020.228708.

[11] J. Li, C. Daniel, and D. Wood, “Materials processing for lithium-ion batteries,” *J. Power Sources*, vol. 196, no. 5, pp. 2452–2460, 2011, doi: 10.1016/j.jpowsour.2010.11.001.

[12] A. Eftekhari, “Lithium-Ion Batteries with High Rate Capabilities,” *ACS Sustain. Chem. Eng.*, vol. 5, no. 4, pp. 2799–2816, 2017, doi: 10.1021/acssuschemeng.7b00046.

[13] R. Moshtev and B. Johnson, “State of the art of commercial Li ion batteries,” *J. Power Sources*, vol. 91, no. 2, pp. 86–91, 2000, doi: 10.1016/S0378-7753(00)00458-4.

[14] H. Liu, Y. Yang, and J. Zhang, “Reaction mechanism and kinetics of lithium ion battery cathode material LiNiO2 with CO2,” *J. Power Sources*, vol. 173, no. 1, pp. 556–561, 2007, doi: 10.1016/j.jpowsour.2007.04.083.

[15] M. Wakihara, “Recent developments in lithium ion batteries,” *Mater. Sci. Eng. R Reports*, vol. 33, no. 4, pp. 109–134, 2001, doi: 10.1016/S0927-796X(01)00030-4.

[16] J. Wen, Y. Yu, and C. Chen, “A review on lithium-ion batteries safety issues: Existing problems and possible solutions,” *Mater. Express*, vol. 2, no. 3, pp. 197–212, 2012, doi: 10.1166/mex.2012.1075.

[17] R. T. L. Ng and M. H. Hassim, “Strategies for assessing and reducing inherent occupational health hazard and risk based on process information,” *Process Saf. Environ. Prot.*, vol. 97, pp. 91–101, 2015, doi: 10.1016/j.psep.2015.03.014.

[18] D. Ren, X. Feng, L. Lu, X. He, and M. Ouyang, “Overcharge behaviors and failure mechanism of lithium-ion batteries under different test conditions,” *Appl. Energy*, vol. 250, no. April, pp. 323–332, 2019, doi: 10.1016/j.apenergy.2019.05.015.

[19] P. G. Balakrishnan, R. Ramesh, and T. Prem Kumar, “Safety mechanisms in lithium-ion batteries,” *J. Power Sources*, vol. 155, no. 2, pp. 401–414, 2006, doi: 10.1016/j.jpowsour.2005.12.002.

[20] Q. F. Yuan, F. Zhao, W. Wang, Y. Zhao, Z. Liang, and D. Yan, “Overcharge failure

investigation of lithium-ion batteries," *Electrochim. Acta*, vol. 178, pp. 682–688, 2015, doi: 10.1016/j.electacta.2015.07.147.

[21] A. Vassighi and M. Sachdev, "Thermal runaway in integrated circuits," *IEEE Trans. Device Mater. Reliab.*, vol. 6, no. 2, pp. 300–305, 2006, doi: 10.1109/TDMR.2006.876577.

[22] Q. Wang, P. Ping, X. Zhao, G. Chu, J. Sun, and C. Chen, "Thermal runaway caused fire and explosion of lithium ion battery," *J. Power Sources*, vol. 208, pp. 210–224, 2012, doi: 10.1016/j.jpowsour.2012.02.038.

[23] X. Feng, M. Ouyang, X. Liu, L. Lu, Y. Xia, and X. He, "Thermal runaway mechanism of lithium ion battery for electric vehicles: A review," *Energy Storage Mater.*, vol. 10, no. May 2017, pp. 246–267, 2018, doi: 10.1016/j.ensm.2017.05.013.

[24] N. E. Galushkin, N. N. Yazvinskaya, and D. N. Galushkin, "Mechanism of Thermal Runaway in Lithium-Ion Cells," *J. Electrochem. Soc.*, vol. 165, no. 7, pp. A1303–A1308, 2018, doi: 10.1149/2.0611807jes.

[25] R. Saada, D. Patel, and B. Saha, "Causes and consequences of thermal runaway incidents - Will they ever be avoided?," *Process Saf. Environ. Prot.*, vol. 97, pp. 109–115, 2015, doi: 10.1016/j.psep.2015.02.005.

[26] L. Huang, Z. Zhang, Z. Wang, L. Zhang, X. Zhu, and D. D. Dorrell, "Thermal runaway behavior during overcharge for large-format Lithium-ion batteries with different packaging patterns," *J. Energy Storage*, vol. 25, no. June, p. 100811, 2019, doi: 10.1016/j.est.2019.100811.

[27] D. Kong, G. Wang, P. Ping, and J. Wen, "Numerical investigation of thermal runaway behavior of lithium-ion batteries with different battery materials and heating conditions," *Appl. Therm. Eng.*, vol. 189, no. January, p. 116661, 2021, doi: 10.1016/j.applthermaleng.2021.116661.

[28] X. Feng *et al.*, "Investigating the thermal runaway mechanisms of lithium-ion batteries based on thermal analysis database," *Appl. Energy*, vol. 246, no. April, pp. 53–64, 2019, doi: 10.1016/j.apenergy.2019.04.009.

[39] D. Ren *et al.*, “A comparative investigation of aging effects on thermal runaway behavior of lithium-ion batteries,” *eTransportation*, vol. 2, p. 100034, 2019, doi: 10.1016/j.etran.2019.100034.

[30] P. Jindal, B. S. Kumar, and J. Bhattacharya, “Coupled electrochemical-abuse-heat-transfer model to predict thermal runaway propagation and mitigation strategy for an EV battery module,” *J. Energy Storage*, vol. 39, no. December 2020, p. 102619, 2021, doi: 10.1016/j.est.2021.102619.

[31] P. Ping, Q. Wang, P. Huang, J. Sun, and C. Chen, “Thermal behaviour analysis of lithium-ion battery at elevated temperature using deconvolution method,” *Appl. Energy*, vol. 129, pp. 261–273, 2014, doi: 10.1016/j.apenergy.2014.04.092.

[32] T. Inoue and K. Mukai, “Roles of positive or negative electrodes in the thermal runaway of lithium-ion batteries: Accelerating rate calorimetry analyses with an all-inclusive microcell,” *Electrochem. commun.*, vol. 77, pp. 28–31, 2017, doi: 10.1016/j.elecom.2017.02.008.

[33] S. Wilke, B. Schweitzer, S. Khateeb, and S. Al-Hallaj, “Preventing thermal runaway propagation in lithium ion battery packs using a phase change composite material: An experimental study,” *J. Power Sources*, vol. 340, pp. 51–59, 2017, doi: 10.1016/j.jpowsour.2016.11.018.

[34] X. Feng, D. Ren, X. He, and M. Ouyang, “Mitigating Thermal Runaway of Lithium-Ion Batteries,” *Joule*, vol. 4, no. 4, pp. 743–770, 2020, doi: 10.1016/j.joule.2020.02.010.

[35] Y. Bai, Q. Chang, Q. Yu, S. Zhao, and K. Jiang, “A novel approach to improve the electrochemical performances of layered LiNi1/3Co1/3Mn1/3O2 cathode by YPO4 surface coating,” *Electrochim. Acta*, vol. 112, pp. 414–421, 2013, doi: 10.1016/j.electacta.2013.09.002.

[36] P. Guan *et al.*, “Recent progress of surface coating on cathode materials for high-performance lithium-ion batteries,” *J. Energy Chem.*, vol. 43, pp. 220–235, 2020, doi: 10.1016/j.jechem.2019.08.022.

[37] R. EL Khalfaouy *et al.*, “Nickel-substituted LiMnPO4/C olivine cathode material:

Combustion synthesis, characterization and electrochemical performances," *Ceram. Int.*, vol. 45, no. 14, pp. 17688–17695, 2019, doi: 10.1016/j.ceramint.2019.05.336.

[38] D. D. MacNeil, D. Larcher, and J. R. Dahn, "Comparison of the Reactivity of Various Carbon Electrode Materials with Electrolyte at Elevated Temperature," *J. Electrochem. Soc.*, vol. 146, no. 10, pp. 3596–3602, 1999, doi: 10.1149/1.1392520.

[39] M. Schmidt *et al.*, "Lithium fluoroalkylphosphates: A new class of conducting salts for electrolytes for high energy lithium-ion batteries," *J. Power Sources*, vol. 97–98, pp. 557–560, 2001, doi: 10.1016/S0378-7753(01)00640-1.

[40] J. H. Shin, W. A. Henderson, and S. Passerini, "Ionic liquids to the rescue? Overcoming the ionic conductivity limitations of polymer electrolytes," *Electrochem. commun.*, vol. 5, no. 12, pp. 1016–1020, 2003, doi: 10.1016/j.elecom.2003.09.017.

[41] Q. Li *et al.*, "Numerical investigation of thermal runaway mitigation through a passive thermal management system," *J. Power Sources*, vol. 429, no. April, pp. 80–88, 2019, doi: 10.1016/j.jpowsour.2019.04.091.

[42] D. Ouyang, M. Chen, Q. Huang, J. Weng, Z. Wang, and J. Wang, "A Review on the thermal hazards of the lithium-ion battery and the corresponding countermeasures," *Appl. Sci.*, vol. 9, no. 12, 2019, doi: 10.3390/app9122483.

[43] S. K. Mohammadian, Y. L. He, and Y. Zhang, "Internal cooling of a lithium-ion battery using electrolyte as coolant through microchannels embedded inside the electrodes," *J. Power Sources*, vol. 293, pp. 458–466, 2015, doi: 10.1016/j.jpowsour.2015.05.055.

[44] M. Winter, B. Barnett, and K. Xu, "Before Li Ion Batteries," *Chem. Rev.*, vol. 118, no. 23, pp. 11433–11456, Dec. 2018, doi: 10.1021/ACS.CHEMREV.8B00422.

[45] K. M. Abraham, "Rechargeable Batteries for the 300-Mile Electric Vehicle and Beyond," *ECS Trans.*, vol. 41, no. 31, pp. 27–34, May 2012, doi: 10.1149/1.3702853/XML.

[46] P. Huang, Q. Wang, K. Li, P. Ping, and J. Sun, "The combustion behavior of large

scale lithium titanate battery," *Sci. Rep.*, vol. 5, 2015, doi: 10.1038/SREP07788.

[47] "Lithium-ion Battery Future Trend India No 1 EV Business Consultan." https://evolt.aevt.org/news/view/11 (accessed Jul. 04, 2022).

[48] S. Ansari *et al.*, "Data-Driven Remaining Useful Life Prediction for Lithium-Ion Batteries Using Multi-Charging Profile Framework: A Recurrent Neural Network Approach," 2021, doi: 10.3390/su132313333.

[49] X. Feng, M. Ouyang, X. Liu, L. Lu, Y. Xia, and X. He, "Thermal runaway mechanism of lithium ion battery for electric vehicles: A review," *Energy Storage Mater.*, vol. 10, pp.

Chapter 2: Literature Review

2.1 Solid electrolyte

Solid-state electrolytes are not flammable and provide superior thermal stability when compared to liquid electrolytes. This results in enhanced safety when compared to batteries that use liquid electrolytes. In addition, their capability of facilitating the use of a Li metal anode with a large capacity has the potential to significantly improve the energy and power density as well as the cycle life of existing batteries [1]. Therefore, it is imperative to replace liquid electrolytes with high-performance solid electrolytes in order to overcome the related safety issues that are associated with conventional batteries, as well as to improve their energy density by enabling the use of high energy density electrodes. This can be accomplished by improving the performance of the solid electrolytes [2].

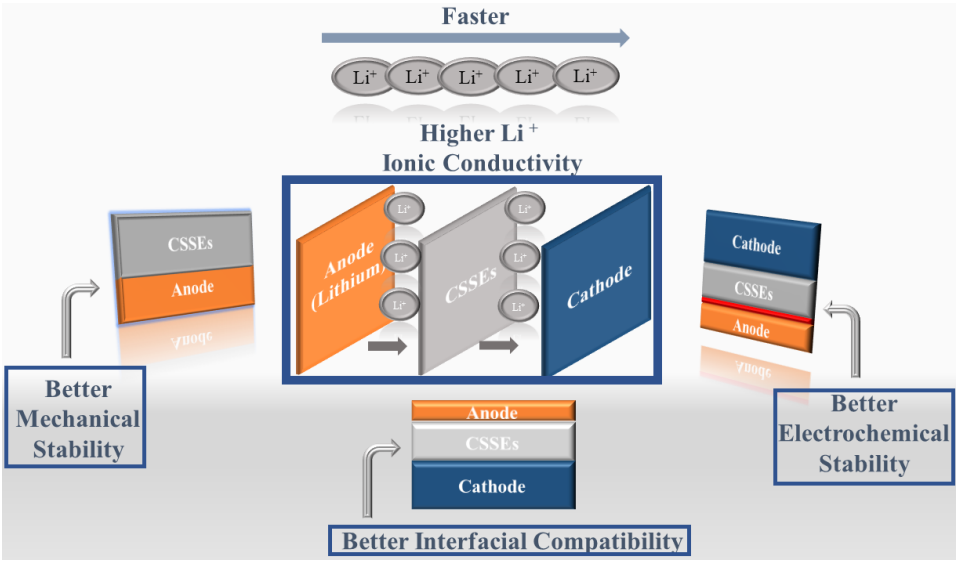

Figure 2-1. Schematic of composite solid-state electrolyte and their features in Li-ion batteries.

Ionic conductivity of solid electrolytes is comparable to that of liquid electrolytes (> 10^{-2} S cm^{-1} at room temperature), a name given to them as "superfast ionic conductors" (SICs). There is no electronic conductivity in solid electrolytes because they are ionic [3]. Lithium dendrites are less likely to form in these electrolytes, which is good for the battery's

performance while also eliminating the flammability and leakage problems associated with liquid electrolytes. All solid-state lithium batteries rely on solid electrolyte as their primary electrolyte (ASSLBs) [4]. Advanced ASSLBs are widely regarded as the most promising future technology for energy storage because they have a higher energy density than ordinary metal ion batteries. In terms of energy density, compactness, stability, and safety, ASSLBs outperform conventional energy storage devices [5].

2.1.1 Background of ASSLBs

A silver-based solid ionic conductor was used in the development of the first solid-state battery in 1950. The battery's internal resistance was quite high, and its current density was extremely poor. As an anode material, silver had a poor electrochemical performance, but it also had a long shelf life and tremendous mechanical strength [6]. Afterwards, Oak Ridge National Laboratory created a thin film LIB version of the current solid-state battery in 1990. An ASSLB with a composite cathode material was created in 2003 by the University of Colorado Boulder. Dyson Ltd. released a high-density ASSLB for commercial use in 2004. In a similar vein, in 2017 a novel ASSLB was developed employing an alkali metal anode and glass electrolyte [7].

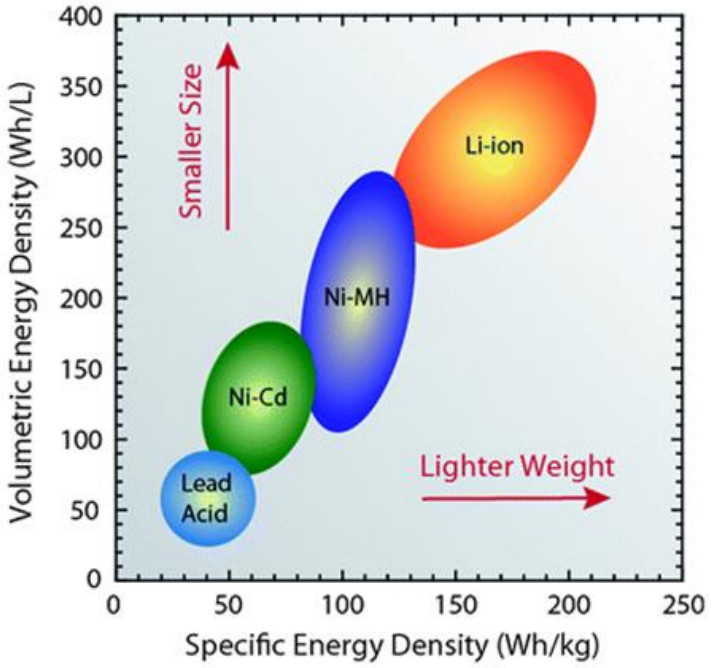

Figure 2-2. Energy density plot of different Battery system [7].

2.2 Types of Solid electrolytes

There are three types of solid electrolytes: polymers, inorganics, and composites. A variety of polymer and inorganic electrolytes are available, including PVF (vinylidene fluoride), PMM (polymethyl methacrylate), PEO (polyethylene oxide), and composites made of both polymer and ceramic materials [8]. In contrast, sulfide-based electrolytes are extremely volatile in the presence of air and moisture, necessitating further handling. Many attempts have been made to produce oxide-based solid ionic conductors because of their characteristics, including NASICON type, LISICON-like sulphide electrolytes, perovskites and garnet-based LLTO and LLZO electrolytes. Composite solid electrolytes, combine the benefits of ceramic and polymer to develop a high-conductive, mechanically durable, readily manufactured solid electrolyte by dispersing ceramic particles in a polymer matrix [10-15].

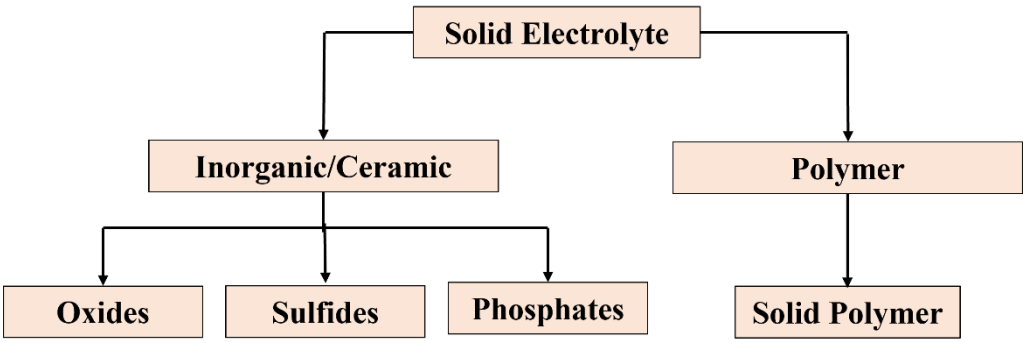

Figure 2-3. Types of solid electrolytes.

2.2.1 Inorganic solid electrolytes

Amorphous (glass) and crystalline forms predominate in inorganic electrolytes, also known as ceramic electrolytes, which are capable of conducting lithium ions. Inorganic SSEs have the highest ionic conductivities and thermal stability of all SSEs. Inorganics are known as single ion conductors because the number of Li ions that may be transferred is almost equal to one [16]. Ceramics include voids and interstitial regions that allow for ion conduction, unlike liquid electrolytes. Oxides and sulphides are the two main types of inorganic solid electrolytes. Because of their poor contact with the cathode material and low ionic conductivity, certain ceramics, such lithium halides and lithium hydrides, aren't suitable for further study [17]. Ceramics' electrochemical and thermal stability is the most

important quality. A number of these materials, in spite of their strong ionic conductivities and large voltage windows, lose their stability when heated over a certain point. Dendrite development, poor electrochemical performance, and breakdown are all consequences of using these fragile ceramics. Due to the electrolyte's breakdown, the voltage window widens, creating a solid electrode interface layer (SEI). This SEI layer is to blame for the ageing of cells [18].

2.2.1.1 Oxide based solid state electrolytes

The types of oxide based solid state electrolytes are perovskite, LISICON, NASICON, garnet types.

Perovskite

Inaguma et al. made the first perovskite SE, which had a bulk ionic conductivity of 1×10^{-3} S cm^{-1} and a total ionic conductivity of 2×10^{-5} S cm^{-1} at room temperature (LLTO). The A sites of the LLTO crystal structure contain Li and La ions, whereas the B sites contain Ti ions [19-22]. Increases in the lattice parameters may be used to alter the size bottlenecks created by oxygen and lithium ions when they move from one A site to another inside the structure's A site arrays. When Inaguma et al. doped 5 percent Sr at the A site of LLTOA, they created an SSE. Consequently, the bottleneck size was raised, and the overall ionic conductivity was also enhanced, as a result of the higher lattice parameters [23].

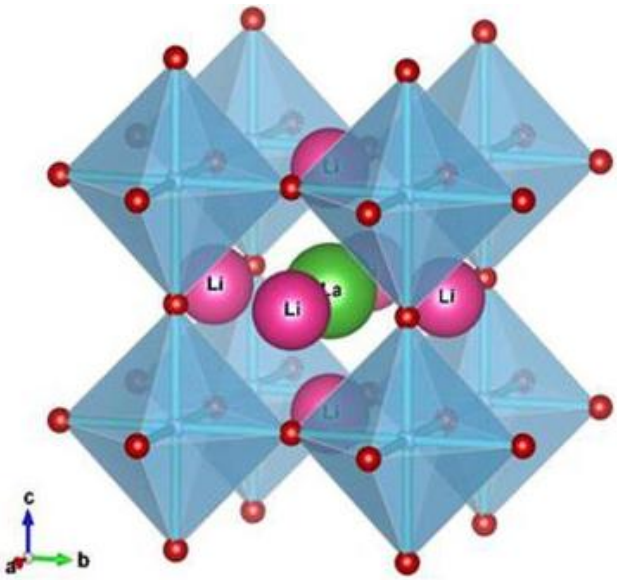

Figure 2-4. Crystal structure of perovskite type solid electrolytes LLTO [23].

As a consequence, it was revealed that the Sr doping resulted in an overall reduction in the number of Li-ion pairs. In spite of its low bulk resistance of 10^{-5} S cm^{-1} at ambient temperature, the grain boundary resistance of LLTO was greater and therefore the high total resistance. Lithium metal anodes were discovered to be incompatible with the low 1.8 V LLTO voltage level that was shown to be unstable. Ti^{+4} low voltage reduction created the structure's instability [24]. Chung et al. used Sn^{+4}, Zr^{+4}, Mn^{+4}, and Ge^{+4} to work on this problem. To prevent the production of impurity phases, the ionic conductivity of Mn and Ge was enhanced. However, the residual Ti was still able to diminish, despite the fact that Ti was just supplemented and not completely replaced. Because of the oxidation states of Zr and Ta, Thangaduari et al. Sr and Zr doped LTO structure was stable with lithium metal [25]. To increase the conductivity, the ionic conductivity has to be increased. According to Cheng et al., the ionic conductivity of LSTZ ($Li_{3/8}$ $Sr_{7/16}$ $Ta_{3/4}$ $Zr_{1/4}$ O_3) synthesized from pristine SSE was 2×10^{-4} S cm^{-1}. LSTZ's grain conductivity was greater than LLTO SSE's and it was proven to be stable at low voltages [26-30].

LISICON

To start, researchers from Hong et al. found that the electrolyte $Li_{1.4}$ $Zn(GeO_4)_4$ has an ionic conductivity of 1.25×10^{-1} S cm^{-1} at temperatures over 100 degrees . Li ion conduction was influenced by two factors: bonding energy and channel size. $[Li_{1.1}Zn(GeO_4)]^{-3}$ serves as the network in this structure, while the remaining three Li ions are free to migrate [31]. When it comes to Li, Zn, and Ge, the O^{-2} forms strong connections, but only weak ones with the other three. Due to the parallelogram shape of the channels, Li ions may travel freely only in two directions. To increase the ionic conductivity, these ions are located in the 4c and 4a positions inside the structure and may diffuse via gaps and interstitials. While this LISICON solid state electrolytes has a low ionic conductivity, it is still being explored further [32].

Lithium orthosilicate, lithium phosphate, and $Li_{4-x}Si_{1-x}P_xO_4$ were all synthesized by Hue et al. Substituting cation Si with lithium ions interstitial to phosphorus ions at concentrations of x=0.5 and x=0,4 resulted in the best ionic conductivity. At these concentrations, however, there was a structural shift [33]. Electrolytes with ionic conductivities of 1.03×10^{-5} S cm^{-1} and 3.7×10^{-5} S cm^{-1} were synthesized by Song et al.

from partly doped oxygen O^{-1}, chlorine Cl^{-1}, $Li_{10.42}Si_{1.5}$ $P_{0.5}Cl_{0.08}O_{11.92}$ and $Li_{10.42}Ge_{1.5}P_{0.5}C_{l0.08}O_{11.92}$, respectively.

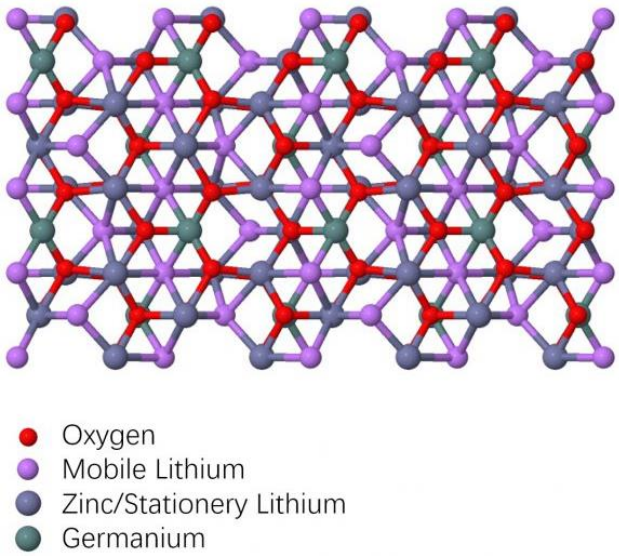

Figure 2-5. Crystal structure of LISICON type solid electrolytes [32].

Because the lattice volume of channels rises due to the increased size of Cl^{-1}, the link between Li and Cl weakens, allowing Li ions to be released for conduction. Low ionic conductivities have prevented LISICON from being used in ASSLBs [34]. As revealed by Kamaya et al., substituting O^{-2} for S^{-2} in the structure increases the ionic conductivity because of the strong connection between lithium and O^{-2} .

Garnet type solid state electrolytes

$Li_3Ln_3M_2O_{12}$ where Ln=Yb, Lu, Gd, Y and M=W and Te was synthesized in 1968 for the first garnet-like structure. A change in the lattice properties of the structure occurs when Te is introduced at the Ln site. There is an unstable TeO_6 octahedral structure in $Li_3Ln_3Te_2O_{12}$ with W at the M site, and only a small number of cations can be added. This is in contrast to the stable TeO_6 octahedral structure in $Li_3Ln_3W_2O_{12}$ with W at the M site [35]. There is a novel garnet structure with Nb and Ta at the M site and La at the Ln site, as described by Thangadurai et al. In the 10^{-6} S cm^{-1} region, high ionic conductivity has been found for room temperature materials. It has a higher ionic conductivity than Ta-doped $Li_3La_3Nb_2O_{12}$, but it is more stable with Li metal since it has a lower reduction potential [36]. A 3D framework for the transport of lithium ions is present in these

substances.

Doping strategies have resulted in a variety of structural changes to garnets. The ionic conductivity of Ba-doped $Li_3La_3Ta_2O_{12}$ was comparable to the bulk conductivity of 4×10^{-5} S cm^{-1} at ambient temperature. Another oxide-based electrolyte that has been proven to be better to others is $Li_3SrLa_3Ta_2O_{12}$ oxide [37]. At room temperature, Murugan et al. created a novel SSE by totally substituting Ta with zirconium Zr $Li_7La_3Zr_2O_{12}$ with a cubic structure that had a conductivity of 3 × 10-4 S cm^{-1}. Some 67% of the Li-ion-occupied Octahedrons in the LLTO structure have been moved from their original positions. While conducting at ambient temperature, 8×10^{-4} S cm^{-1}, the bulk conductivity of LLTO was found to be smaller than the total conductivity of niobium and zirconium doped structures [38].

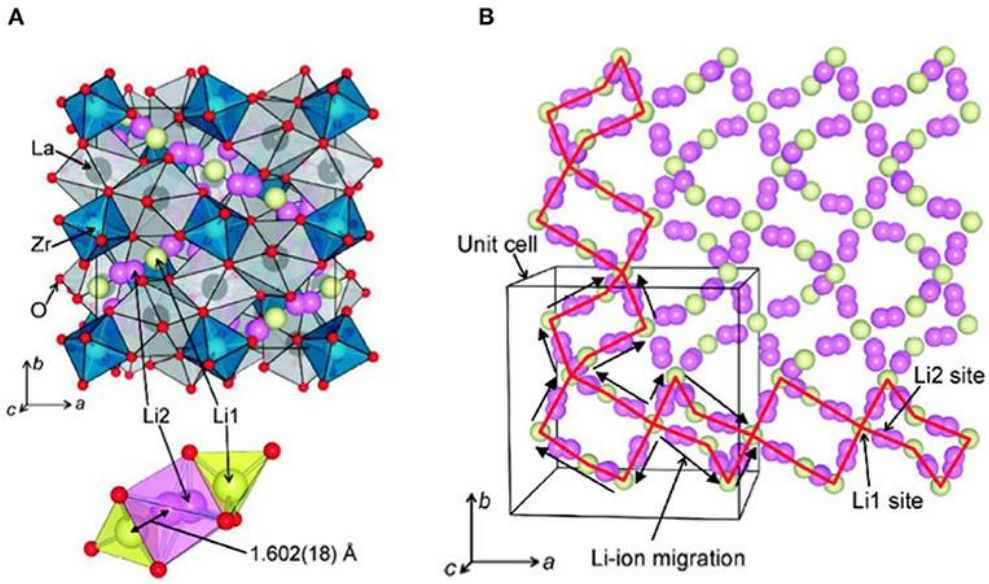

Figure 2-6. Crystal structure of garnet-type LLZO [38].

ASSLB constructed with lithium cobalt cathode and lithium metal anode has a voltage window of 0-9 V, according to the paper. Moisture and CO_2 are big problems for the garnet electrolyte. Stabilizing LLZO garnet has been the subject of recent study [39-44].

NASICON

Sodium super ionic conductor having the general formula $NaM_2(PO_4)_3$ in which M is a positive ion. $Na_{1+x}Zr_2Si_xP_{3-x}O_{12}$ (x=0-3) is an example of a system that uses this kind of formula. Rhombohedral structure may be found in the range 0:3, whereas monoclinic

structure can be found in the region x=1.8:2.2. Oxygen atoms are shared between PO_4 and SiO_4 tetrahedrons and ZrO_6 octahedrons in a 3D framework and pathways [45]. To go from A1 to A2, sodium Na ions have to travel down the c-axis. In the case of x=0, the activation energy for the transfer of mobile ions is larger, but when x>0 the activation energy decreases as spare mobile ions occupy A1 sites. For example, route sizes and diffusion rates are determined by ions' sizes. When compared to Na^+ and O^+ ions, routes have a diameter twice as large. Because of this, framework ions should be viewed in terms of the radius of their Na atoms [46-49]. SSE When heated to high temperatures, the conductivity of $Na_3Zr_2Si_2PO_{12}$ was measured at 2×10^{-1} S cm^{-1}. A monoclinic phase was seen when the $LiZr_2(PO_4)_3$ electrolyte was synthesized at 1200℃, and the ionic conductivity of 3.3×10^{-6} S cm^{-1} was much lower than that of its Na counterpart. High temperatures caused the phase to transition from monocrystal to rhombohedral at 40℃, with a conductivity of 1.2×10^{-2} S cm^{-1}. Additionally, a phase transition from monoclinic to orthorhombic was seen during the low-temperature synthesis [50].

According to Aono et al., the Ti-doped (LTP) NASICON type SSE has the highest ionic conductivity and is the most stable structure for lithium-ion conduction among other dopants. The electrochemical performance of $Li_{1+x}Fe_xHf_{2-x}(PO_4)_3$, $Li_{1+x}Al_xTi_{2-x}(PO_4)_3$ (LATP), and Li_{1+x} $Al_xGe_{2-x}(PO_4)_3$ is improved by adding trivalent cations Al^{+3} and Fe^{+3} to the M^{+4} site (LAGP). These three structures have an ionic conductivity of more than 10^{-4} S cm^{-1}. Conductivity of $Li_{1.3}$ $Al_{0.3}Ti_{1.7}(PO_4)_3$ was 7×10^{-4} S cm^{-1} at ambient temperature, although in the structure Ti^{+4} decreases and due to that low stability. Consequently, the stability of $Li_{1+x}Fe_xHf_{2-x}(PO_4)_3$ and $Li_{1+x}Ge_{2-x}(PO_4)_3$ is excellent [51]. Dense electrolytes with conductivity of 3×10^{-4} S cm^{-1} for LTP-$0.2Li_3BO_3$ are produced by doping lithium phosphate Li_3PO_4 and lithium borate Li_3BO_3.

LATP and LAGP solid state electrolytes are two well investigated NASICON type SSE types. As a result of a decrease in Ti^{+4}, LATP NASICON's strong ionic conductivity is incompatible with electrode materials, particularly lithium metal as an anode [52]. To address this problem, lithium addition to LTP was performed, resulting in the synthesis of two electrolytes: LTP and $Li_3Ti_2(PO_4)_3$, both of which exhibited rhombohedral structures, but the distribution of Li ions in each was different. There is lithium at A1 site in LTP, while A2 site is vacant in $Li_3Ti_2(PO_4)_3$, but A1 site is occupied in $Li_3Ti_2(PO_4)_3$. The c-axis

repulsions with octahedrons also rose as a consequence of this distribution [53].

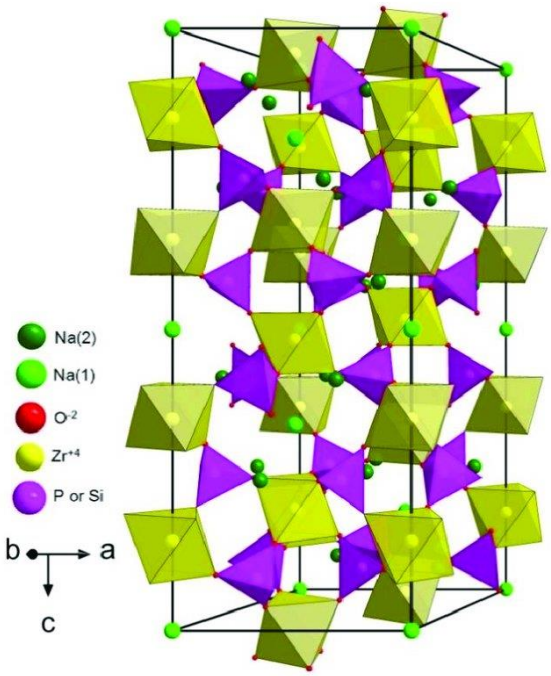

Figure 2-7. Rombohedral NASICON crystal structure [1].

Initially, LAGP electrolyte was formed by melting and quenching. At 25 degrees Celsius, the measured ionic conductivity was 4×10^{-4} S cm^{-1}. The conductivity of glass is increased because of the thick structure and intimate contact between the grains. Li_2O was introduced to the $Li_{1+x}Al_xGe_{2-x}(PO_4)_3$ LAGP structure with x=0.5 by another scientist. At room temperature, the grain and total conductivity values were 1.18×10^{-3} S cm^{-1} and 7.25×10^{-4} S cm^{-1}, respectively, of the lithium secondary phases that helped crystallize the glass and so enhanced the conductivity. The electrolyte proved very stable at 6 volts, both electrochemically and thermally. When the temperature was raised above 900 ℃, another impurity phase $AlPO_4$ developed, which interacted with lithium and reduced the amount of mobile lithium ions, higher temperature sintering exhibited strong ionic conductivities. High ionic conductivity, broad voltage range, and great electrochemical stability make LAGP one among the best NASICON solid state electrolytes. However, its usage in ASSLBs is restricted because of the high cost of the basic element GeO_2. An inexpensive substitute for germanium may make this electrolyte suitable for ASSLBs [54].

2.2.1.2 Sulfide based solid state electrolytes

Many studies have been done on solid-state batteries, with sulfide being one of the most promising materials. This substance's strong conductivity and broad potential window make it an ideal electrochemical candidate. In compared to more traditional electrolytes like liquid and oxide solid, sulfide demonstrated a high-performance solid-state lithium metal battery. The mechanical properties of sulfide solid electrolytes are superior than other electrolytes. It is possible to make sulfide solid electrolytes from a variety of different materials, including argyrodite (Li_6PS_5X), lithium phosphorus sulfur (LPS) sulfides, and thio-LISICONs. There are three classifications of sulfide based solid state electrolytes including LPS, Li_6PS_5X (X: Cl, Br, and I) and $Li_xMP_xS_x$ (M: Ge, Sn, Si, and Al). In general, three processes are used to synthesize sulfide solid electrolyte: melting, ball milling, and wet chemical. Heat is applied to the melting point of the material to be quenched, and then the temperature is rapidly reduced [55]. A popular type of mechanical high-energy milling involving complicated processes like as mixing and solid-state reactions is ball milling, which is the most often used approach. A wet chemical is one that is synthesized using a solution in a process. Research on the electrochemical conductivity, stability, and performance of sulfide solid electrolytes is also necessary in order to determine which sulfide base solid electrolyte is most likely to be created [56].

LPS

The lithium thiophosphate, often known as the LPS class, is a group of compounds that conduct electricity very well. There have been many different crystalline phases of sulfide identified, and the kind of crystal that forms is determined by the heat treatment that is used as well as the composition of the glass that is produced [57]. The following crystalline phases are considered to be sulfide: Li_3PS_4, $Li_7P_3S_{11}$, and $Li_4P_2S_6$. Ionic conductivity was substantially reduced owing to the creation of individual crystals, and the composition of the glass that developed in the LPS has an effect on how that conductivity changes.

Li_6PS_5X (X: Cl, Br, and I)

One form of sulfide solid electrolyte is known as lithium argyrodites Li_6PS_5X (X: Cl, Br, and I). At 298 Kelvin, these lithium argyrodites have a relatively high ionic conductivity,

with values ranging from 10^{-2} to 10^{-3} S cm^{-1} for Br and Cl respectively. It has been shown that the increase in conductivity may be attributed to the incorporation of anions into the solid electrolyte. The two most essential characteristics that determine conductivity are the size of the anions that are coordinated to the mobile cations and their capacity to be polarized. This section provides an explanation of various different forms of Li-argyrodites solid electrolytes that are sulfide-based, including Li_6PS_5Cl, Li_6PS_5Br, and Li_6PS_5I [58].

LixMPxSx (M: Ge, Sn, Si, and Al)

A group of solid electrolytes that have favorable properties may be described as the ceramic thio-LISICON group. LixMPxSx is a derivation of this group. The L-P-S system may also be derived in the form of LixMPxSx. The first LixMPxSx group, known as $Li_{10}GeP_2S_{12}$ (LGPS), was produced as a consequence of the creation of the LiS-PS form of the system, which was found to feature Li_3PS_4 and Li_4GeS_4 structures. This led to the discovery of the LiS-PS form of the system. The high ionic conductivity of ceramic-sulfide solids, such as Li10GeP2S12 (LGPS), has attracted a lot of attention recently due to the fact that it ranges from 1–25 mS cm^{-1}. There are several drawbacks associated with the presence of Ge in $Li_{10}GeP_2S_{12}$ in terms of the availability and cost of materials. $Li_{10}GeP_2S_{12}$ can be made without the Ge component, but there are various more options. If you want to substitute Ge for Sn, Si, or Al in LGPS's chemical formula (LixMPxSx), you may do so. The ionic conductivity of $Li_{10}GeP_2S_{12}$ (LGPS) has been studied further and reveals very high values. Other alternatives must be found in order to produce at a reduced cost since the price of Ge is expensive and its supply is restricted. Because they have a similar polygon structure, other alternatives that are employed include tin, silicon, and aluminum [59]. There are numerous other kinds of solid electrolytes that are based on sulfides, including $Li_{10}GeP_2S_{12}$, $Li_{10}SnP_2S_{12}$, and $Li_{10}SiP_2S_{12}$, in addition to $Li_{11}AlP_2S_{12}$.

2.2.2 Polymer solid state electrolytes

Lithium salts may be incorporated into polymer materials in the form of solid polymer electrolytes. Lithium metal salt was initially incorporated into polyethylene oxide (PEO), which has been extensively explored. Liquid hosts cannot be added to PEO to ensure leak-free operation. Although polymer electrolyte materials are flexible, safe, and compatible,

their poor mechanical strength and dendrite formation restrict their usage in ASSLBs, as their ionic conductivity is in the range of 10^{-6}-10^{-8} S cm^{-1}. In several research, the combination of polymers and other materials has resulted in an increased performance as a consequence of these constraints [60]. Composite solid-state electrolytes (CSSEs) are a novel kind of electrolyte that is being examined for future ASSLBs. Toyota has announced the manufacturing of a new electric vehicle (EV) based on ASSLB (CSSEs) in the mid-2020s. We may classify CSSEs according to the following three classifications:

- Inorganic- organic
- Organic-organic
- Inorganic-inorganic.

The inorganic/polymer electrolytes are the most promising and have received the greatest research attention. In LIBs, CSSEs are structured as follows:

- Polymer filled inorganic 3D framework
- Layered structures
- Composite electrolytes with open framework
- Polymer matrix incorporating inorganic fillers

2.2.2.1 Polymer filled inorganic 3D framework

High ionic conductivity is achieved via fillers in the polymer matrix, which inhibits crystal formation. Increasing the electrochemical performance of the inorganic fibers and rods is currently the focus of many studies. These polymer-filled 3D inorganic frameworks offer more pathways for lithium ion hopping than nanorod and wire structures. Sol-gel and heat treatments are used to create these structures. Polymer was then added to the framework by J. Bae et al. via the sol-gel process, creating a 3D structure of inorganic LLTO. At room temperature, the corresponding ionic conductivity was 8.8×10^{-5} S cm^{-1} [61].

2.2.2.2 Layered structures

An important feature of CSSEs' multi-layered structure is that it allows researchers to examine the pros and cons of lithium ion hopping in each layer, thanks to the inclusion of inorganic fillers in the polymer matrix [62]. Ionic conductivity and mechanical strength are both improved, as is the interfacial contact between electrode and electrolyte surface, thanks to these structures Based on the study of a group of experts, the layered structures

are primarily split into two categories: double layered and sandwich structure. The polymer layer serves as a solid interface layer between the inorganic pellet and the Li metal anode in a double layered configuration. Dendrite development is reduced and interfacial resistance between contacts is reduced by this layer [63]. The soft polymer interface is employed between the electrodes and the electrolyte in the sandwich structure electrolyte. Interfacial contact was reduced by W. Zhou's CSSE, which had a ceramic layer ($L_{1.3}Al_{0.3}Ti_{1.7}(PO_4)_3$) sandwiched between two polymer layers (PEO and PEMA).

2.2.2.3 Composite electrolytes with open framework

Materials called Metal Oxide Frameworks (MOFs) consist of metal centers linked together by organic linkers to form three-dimensional structures. As empty spaces grow inside the organic molecules' coordination network, there may be thousands of square meters of surface area per gram in certain MOFs. Recently, they've been employed as catalysts, electrode material and electrolytes in electrochemical systems. MOF-activated carbon compositions were made by Fleker et al. to discuss the nonconductive character of MOFs due to the network's coordinating bonds [64]. Carbon activated MOF nanoparticles display an intriguing EPR signal. Redox coupling Cu^{2+}/Cu^{+} in MOF enhances AC capacitance by 30 percent. The formation of MOF on graphene sets was thoroughly investigated by Yaghi et al. in their work. Over 10,000 charge/discharge cycles, zirconium-MOF demonstrated an aerial capacitance of 5.09 F cm^{-1}. Polymer matrix dipped in MOF fillers combined with Li salts is the MOF version of CSSEs. An SSE-incorporating cell and MOF filler with a LiTFSi polymer matrix were created by H. Huo et al. According to the results, it had a much greater ionic conductivity than the pristine electrolyte complex (3.65×10^{-5} S cm^{-1}). CSSEs of this sort have been extensively studied using Mg-TPA and Al-TPA-MOF as research subjects.

2.2.2.4 Polymer matrix incorporating inorganic fillers

Inorganic fillers are classified as either active or passive based on their ionic conductivities. A complex production process makes it unable to tune the active's ionic conductivities or Li^{+} transference numbers with the polymer matrix. Moisture and CO_2 are critical to the performance of active fillers. Despite their poor conductivities and high

interfacial resistance, passive fillers are low-cost, simple to handle, and adjustable in matrix.

The addition of passive fillers in the polymer matrix is the most commonly investigated CSSE to improve electrochemical performance, mechanical strength and thermal stability. There are two types of passive fillers: metal oxide fillers and non-metal oxide fillers. The metal oxide fillers include aluminum oxide Al_2O_3, titanium oxide TiO_2, silicon dioxide SiO_2 and zirconium oxide ZrO_2 among other materials. The conductivity of Al_2O_3 is almost unchanged, while the composite electrolyte's mechanical strength increases [65]. Lithium ions move more easily through TiO_2, resulting in greater ionic conductivity. It's true that carbon isn't employed in electrolytes because of its electrical characteristics, but the insertion of even a little amount into the PEO matrix led to a significant increase in surface area and an increase in ionic conductivity, making it an excellent anode material. Sand, clay, zeolite, and nonporous materials are also used as non-metal fillers. When more metal oxide fillers are added to a polymer matrix, agglomeration ensues. Composites' ionic conductivities are unaffected by the ratio of components. 1D filler may minimize agglomeration by providing a longer dimension for 0D metal oxide filler.

A higher ionic conductivity may be achieved with active fillers than with passive fillers, and more filler material can be added to the matrix rather than raising the fraction ratio of filler, increasing the contact area but decreasing the ionic conductivity. A polymer matrix containing the gallium-based garnet electrolyte Ga-LLZO produces a space charge zone with strong ionic conductivity. Defects in the Ga-LLZO surface cause this area to form. The template solution approach is used to make the active fillers that are one- and two-dimensional. Incorporating these fillers into polymer matrices necessitates a variety of production processes. Liu et al. employ the electrospinning technique to make CSSE from perovskites LLTO electrolyte precursors calcined from PVP fibers. The structure's vacancies encourage Li+ ion hopping, boosting ionic conductivity [65].

Summary

In this chapter review of the literature on electrolyte materials, types for ASSLBs is discussed. Also mentioned in this section is how the solid-state electrolytes work. Additional information on oxide-based electrolyte materials and their advantages for energy storage applications is also provided.

References

[1] R. Chen, W. Qu, X. Guo, L. Li, and F. Wu, “The pursuit of solid-state electrolytes for lithium batteries: From comprehensive insight to emerging horizons,” *Mater. Horizons*, vol. 3, no. 6, pp. 487–516, 2016, doi: 10.1039/C6MH00218H.

[2] A. Yoshino, *Development of the Lithium-Ion Battery and Recent Technological Trends*. Elsevier, 2014. doi: 10.1016/B978-0-444-59513-3.00001-7.

[3] Y. Liu, R. Zhang, J. Wang, and Y. Wang, “Current and future lithium-ion battery manufacturing,” *iScience*, vol. 24, no. 4, p. 102332, 2021, doi: 10.1016/j.isci.2021.102332.

[4] A. Eftekhari, “Lithium-Ion Batteries with High Rate Capabilities,” *ACS Sustain. Chem. Eng.*, vol. 5, no. 4, pp. 2799–2816, 2017, doi: 10.1021/acssuschemeng.7b00046.

[5] L. Yue *et al.*, “All solid-state polymer electrolytes for high-performance lithium ion batteries,” *Energy Storage Mater.*, vol. 5, pp. 139–164, 2016, doi: 10.1016/j.ensm.2016.07.003.

[6] Y. Zhao *et al.*, “A new solid polymer electrolyte incorporating Li 10 GeP 2 S 12 into a polyethylene oxide matrix for all-solid-state lithium batteries,” vol. 301, pp. 47–53, 2016, doi: 10.1016/j.jpowsour.2015.09.111.

[7] W. Xiao *et al.*, “High performance composite polymer electrolytes doped with spherical-like and honeycomb structural Li0.1Ca0.9TiO3 particles,” *Front. Chem.*, vol. 6, no. OCT, pp. 1–10, 2018, doi: 10.3389/fchem.2018.00525.

[8] J. Bae *et al.*, “A 3D Nanostructured Hydrogel-Framework-Derived High-Performance Composite Polymer Lithium-Ion Electrolyte,” *Angew. Chemie - Int. Ed.*, vol. 57, no. 8, pp. 2096–2100, 2018, doi: 10.1002/anie.201710841.

[9] S. Chen *et al.*, “Sulfide solid electrolytes for all-solid-state lithium batteries: Structure, conductivity, stability and application,” *Energy Storage Mater.*, vol. 14, no. February, pp. 58–74, 2018, doi: 10.1016/j.ensm.2018.02.020.

[10] Y. Sun, K. Suzuki, S. Hori, M. Hirayama, and R. Kanno, “Superionic Conductors:

Li10+δ[SnySi1-y]1+δP2-δS12 with a Li10GeP2S12-type Structure in the Li3PS4-Li4SnS4-Li4SiS4 Quasi-ternary System," *Chem. Mater.*, vol. 29, no. 14, pp. 5858–5864, 2017, doi: 10.1021/acs.chemmater.7b00886.

[11] Z. Wang, J. Mo, Y. Wu, H. Ye, and X. Wu, "Synthesis of lithium garnet oxides of the compositions series Li7-xLa3Zr2-xTaxO12," *J. Wuhan Univ. Technol. Mater. Sci. Ed.*, vol. 32, no. 6, pp. 1261–1264, 2017, doi: 10.1007/s11595-017-1739-y.

[12] L. Shen *et al.*, "Preparation and characterization of Ga and Sr co-doped Li7La3Zr2O12 garnet-type solid electrolyte," *Solid State Ionics*, vol. 339, no. May, p. 114992, 2019, doi: 10.1016/j.ssi.2019.05.027.

[13] M. Murayama, N. Sonoyama, A. Yamada, and R. Kanno, "Material design of new lithium ionic conductor, thio-LISICON, in the Li2S-P2S5 system," *Solid State Ionics*, vol. 170, no. 3–4, pp. 173–180, 2004, doi: 10.1016/j.ssi.2004.02.025.

[14] C. Shao, Z. Yu, H. Liu, Z. Zheng, N. Sun, and C. Diao, "Enhanced ionic conductivity of titanium doped Li7La3Zr2O12 solid electrolyte," *Electrochim. Acta*, vol. 225, pp. 345–349, 2017, doi: 10.1016/j.electacta.2016.12.140.

[15] J. C. Bachman *et al.*, "Inorganic Solid-State Electrolytes for Lithium Batteries: Mechanisms and Properties Governing Ion Conduction," *Chem. Rev.*, vol. 116, no. 1, pp. 140–162, 2016, doi: 10.1021/acs.chemrev.5b00563.

[16] Y. Zheng *et al.*, "A review of composite solid-state electrolytes for lithium batteries: Fundamentals, key materials and advanced structures," *Chem. Soc. Rev.*, vol. 49, no. 23, pp. 8790–8839, 2020, doi: 10.1039/d0cs00305k.

[17] R. C. Agrawal and G. P. Pandey, "Solid polymer electrolytes: Materials designing and all-solid-state battery applications: An overview," *J. Phys. D. Appl. Phys.*, vol. 41, no. 22, 2008, doi: 10.1088/0022-3727/41/22/223001.

[18] L. C. Charles Hardy and D. F. Shriver, "Preparation and Electrical Response of Solid Polymer Electrolytes with Only One Mobile Species," *J. Am. Chem. Soc.*, vol. 107, no. 13, pp. 3823–3828, 1985, doi: 10.1021/ja00299a012.

[19] K. Murata, S. Izuchi, and Y. Yoshihisa, "Overview of the research and development of solid polymer electrolyte batteries," *Electrochim. Acta*, vol. 45, no. 8, pp. 1501–

1508, 2000, doi: 10.1016/S0013-4686(99)00365-5.

[20] F. Deng *et al.*, "Microporous polymer electrolyte based on PVDF/PEO star polymer blends for lithium ion batteries," *J. Memb. Sci.*, vol. 491, pp. 82–89, 2015, doi: 10.1016/j.memsci.2015.05.021.

[21] A. Bhaskar, J. J. Yuan, and C. J. Liu, "The effects of Si doping on the thermoelectric and magnetic properties of Ca0.98Bi0.02Mn1-xSixO 3-δ with x = 0.00, 0.02 and 0.03," *Mater. Sci. Eng. B Solid-State Mater. Adv. Technol.*, vol. 186, no. 1, pp. 48–53, 2014, doi: 10.1016/j.mseb.2014.03.009.

[22] E. M. Masoud, A. A. El-Bellihi, W. A. Bayoumy, and M. A. Mousa, "Organic-inorganic composite polymer electrolyte based on PEO-LiClO 4 and nano-Al2O3 filler for lithium polymer batteries: Dielectric and transport properties," *J. Alloys Compd.*, vol. 575, pp. 223–228, 2013, doi: 10.1016/j.jallcom.2013.04.054.

[23] M. Ravi, K. Kiran Kumar, V. Madhu Mohan, and V. V. R. Narasimha Rao, "Effect of nano TiO2 filler on the structural and electrical properties of PVP based polymer electrolyte films," *Polym. Test.*, vol. 33, pp. 152–160, 2014, doi: 10.1016/j.polymertesting.2013.12.002.

[24] K. K. Wimalaweera, V. A. Seneviratne, and M. A. K. L. Dissanayake, "EFFECT OF Al 2 O 3 CERAMIC FILLER ON THERMAL AND TRANSPORT PROPERTIES OF POLY(ETHYLENE OXIDE)-LITHIUM PERCHLORATE SOLID POLYMER ELECTROLYTE," *Procedia Eng.*, vol. 215, no. 2017, pp. 109–114, 2017, doi: 10.1016/j.proeng.2018.02.082.

[25] R. Zhang, M. Hummelgård, and H. Olin, "A facile one-step method for synthesising a parallelogram-shaped single-crystalline ZnO nanosheet," *Mater. Sci. Eng. B Solid-State Mater. Adv. Technol.*, vol. 184, no. 1, pp. 1–6, 2014, doi: 10.1016/j.mseb.2013.12.009.

[26] S. A. Hashmi, M. Y. Bhat, M. K. Singh, N. T. K. Sundaram, B. P. C. Raghupathy, and H. Tanaka, "Ionic liquid-based sodium ion-conducting composite gel polymer electrolytes: effect of active and passive fillers," *J. Solid State Electrochem.*, vol. 20, no. 10, pp. 2817–2826, 2016, doi: 10.1007/s10008-016-3284-6.

[27] J. Sharma and S. Hashmi, “Magnesium ion-conducting gel polymer electrolyte nanocomposites: Effect of active and passive nanofillers,” *Polym. Compos.*, vol. 40, no. 4, pp. 1295–1306, 2019, doi: 10.1002/pc.24853.

[28] J. Cui *et al.*, “Solid polymer electrolytes with flexible framework of SiO2 nanofibers for highly safe solid lithium batteries,” *Polymers (Basel).*, vol. 12, no. 6, 2020, doi: 10.3390/POLYM12061324.

[29] S. Sen Chi, Y. Liu, N. Zhao, X. Guo, C. W. Nan, and L. Z. Fan, “Solid polymer electrolyte soft interface layer with 3D lithium anode for all-solid-state lithium batteries,” *Energy Storage Mater.*, vol. 17, no. July 2018, pp. 309–316, 2019, doi: 10.1016/j.ensm.2018.07.004.

[30] J. Bae, Y. Li, F. Zhao, X. Zhou, Y. Ding, and G. Yu, “Designing 3D nanostructured garnet frameworks for enhancing ionic conductivity and flexibility in composite polymer electrolytes for lithium batteries,” *Energy Storage Mater.*, vol. 15, no. March, pp. 46–52, 2018, doi: 10.1016/j.ensm.2018.03.016.

[31] S. Rajendran, M. Sivakumar, and R. Subadevi, “Effect of salt concentration in poly(vinyl alcohol)-based solid polymer electrolytes,” *J. Power Sources*, vol. 124, no. 1, pp. 225–230, 2003, doi: 10.1016/S0378-7753(03)00591-3.

[32] Z. Zhang, Y. Huang, H. Gao, J. Hang, C. Li, and P. Liu, “MOF-derived ionic conductor enhancing polymer electrolytes with superior electrochemical performances for all solid lithium metal batteries,” *J. Memb. Sci.*, vol. 598, no. December 2019, p. 117800, 2020, doi: 10.1016/j.memsci.2019.117800.

[33] M. Yao, T. Yu, Q. Ruan, Q. Chen, H. Zhang, and S. Zhang, “High-Voltage and Wide-Temperature Lithium Metal Batteries Enabled by Ultrathin MOF-Derived Solid Polymer Electrolytes with Modulated Ion Transport,” *ACS Appl. Mater. Interfaces*, vol. 13, no. 39, pp. 47163–47173, 2021, doi: 10.1021/acsami.1c15038.

[34] P. Guo, M. Song, and Y. Wang, “Promising application of MOF as composite solid electrolytes via clathrates of ionic liquid,” *Inorganica Chim. Acta*, vol. 491, no. January, pp. 128–131, 2019, doi: 10.1016/j.ica.2019.02.038.

[35] D. E. Mathew, S. Gopi, M. Kathiresan, A. M. Stephan, and S. Thomas, “Influence

of MOF ligands on the electrochemical and interfacial properties of PEO-based electrolytes for all-solid- state lithium batteries," *Electrochim. Acta*, vol. 319, pp. 189–200, 2019, doi: 10.1016/j.electacta.2019.06.157.

[36] S. K. Fullerton-Shirey and J. K. Maranas, "Effect of LiClO 4 on the structure and mobility of PEO-based solid polymer electrolytes," *Macromolecules*, vol. 42, no. 6, pp. 2142–2156, 2009, doi: 10.1021/ma802502u.

[37] J. Mindemark, M. J. Lacey, T. Bowden, and D. Brandell, "Beyond PEO—Alternative host materials for Li+-conducting solid polymer electrolytes," *Prog. Polym. Sci.*, vol. 81, pp. 114–143, 2018, doi: 10.1016/j.progpolymsci.2017.12.004.

[38] G. M. Wu, S. J. Lin, and C. C. Yang, "Preparation and characterization of PVA/PAA membranes for solid polymer electrolytes," *J. Memb. Sci.*, vol. 275, no. 1–2, pp. 127–133, 2006, doi: 10.1016/j.memsci.2005.09.012.

[39] A. Manthiram, X. Yu, and S. Wang, "Lithium battery chemistries enabled by solid-state electrolytes," *Nat. Rev. Mater.*, vol. 2, no. 4, pp. 1–16, 2017, doi: 10.1038/natrevmats.2016.103.

[40] L. Zhu, P. Zhu, Q. Fang, M. Jing, and X. Shen, "Electrochimica Acta A novel solid PEO / LLTO-nanowires polymer composite electrolyte for solid-state lithium-ion battery," *Electrochim. Acta*, vol. 292, pp. 718–726, 2018, doi: 10.1016/j.electacta.2018.10.005.

[41] S. Y. Jung, R. Rajagopal, and K. S. Ryu, "Synthesis and electrochemical performance of (100−x)Li7P3S11-xLi2OHBr composite solid electrolyte for all-solid-state lithium batteries," *J. Energy Chem.*, vol. 47, pp. 307–316, 2020, doi: 10.1016/j.jechem.2020.02.018.

[42] N. Bonanos, K. S. Knight, and B. Ellis, "Perovskite solid electrolytes: Structure, transport properties and fuel cell applications," *Solid State Ionics*, vol. 79, no. C, pp. 161–170, 1995, doi: 10.1016/0167-2738(95)00056-C.

[43] B. Huang *et al.*, "Li-Ion Conduction and Stability of Perovskite Li3/8Sr7/16Hf1/4Ta3/4O3," *ACS Appl. Mater. Interfaces*, vol. 8, no. 23, pp. 14552–14557, 2016, doi: 10.1021/acsami.6b03070.

[44] K. Kim and D. J. Siegel, “Multivalent Ion Transport in Anti-Perovskite Solid Electrolytes,” *Chem. Mater.*, vol. 33, no. 6, pp. 2187–2197, 2021, doi: 10.1021/acs.chemmater.1c00096.

[45] Y. Li *et al.*, “A Perovskite Electrolyte That Is Stable in Moist Air for Lithium-Ion Batteries,” *Angew. Chemie - Int. Ed.*, vol. 57, no. 28, pp. 8587–8591, 2018, doi: 10.1002/anie.201804114.

[46] K. Liu, M. Wu, L. Wei, Y. Lin, and T. Zhao, “A composite solid electrolyte with a framework of vertically aligned perovskite for all-solid-state Li-metal batteries,” *J. Memb. Sci.*, vol. 610, no. November 2019, p. 118265, 2020, doi: 10.1016/j.memsci.2020.118265.

[47] F. Z. T. Yang, V. K. Peterson, and S. Schmid, “Composition and temperature dependent structural investigation of the perovskite-type sodium-ion solid electrolyte series Na1/2−xLa1/2−xSr2xZrO3,” *J. Alloys Compd.*, vol. 863, p. 158500, 2021, doi: 10.1016/j.jallcom.2020.158500.

[48] H. H. Sumathipala, M. A. K. L. Dissanayake, and A. R. West, “Novel LISICON mixed conductors, $Li_{4-2x}Co_xGeO_4$,” *Solid State Ionics*, vol. 31, no. 86–88, pp. 719–724, 1996, doi: 10.1109/6.249069.

[49] B. Zhang, L. Yang, L. W. Wang, and F. Pan, “Cooperative transport enabling fast Li-ion diffusion in Thio-LISICON Li10SiP2S12 solid electrolyte,” *Nano Energy*, vol. 62, no. May, pp. 844–852, 2019, doi: 10.1016/j.nanoen.2019.05.085.

[50] L. Bi *et al.*, “Critical roles of RuO2 nano-particles in enhancing cyclic and rate performance of LISICON Li3V2(PO4)3 cathode materials,” *J. Alloys Compd.*, vol. 845, p. 156271, 2020, doi: 10.1016/j.jallcom.2020.156271.

[51] N. J. Dudney, “Addition of a thin-film inorganic solid electrolyte (Lipon) as a protective film in lithium batteries with a liquid electrolyte,” *J. Power Sources*, vol. 89, no. 2, pp. 176–179, 2000, doi: 10.1016/S0378-7753(00)00427-4.

[52] Y. Hamon *et al.*, “Influence of sputtering conditions on ionic conductivity of LiPON thin films,” *Solid State Ionics*, vol. 177, no. 3–4, pp. 257–261, 2006, doi: 10.1016/j.ssi.2005.10.021.

[53] K. Senevirathne, C. S. Day, M. D. Gross, A. Lachgar, and N. A. W. Holzwarth, "A new crystalline LiPON electrolyte: Synthesis, properties, and electronic structure," *Solid State Ionics*, vol. 233, pp. 95–101, 2013, doi: 10.1016/j.ssi.2012.12.013.

[54] A. S. Westover, N. J. Dudney, R. L. Sacci, and S. Kalnaus, "Deposition and Confinement of Li Metal along an Artificial Lipon-Lipon Interface," *ACS Energy Lett.*, vol. 4, no. 3, pp. 651–655, 2019, doi: 10.1021/acsenergylett.8b02542.

[55] W. C. West, J. F. Whitacre, and J. R. Lim, "Chemical stability enhancement of lithium conducting solid electrolyte plates using sputtered LiPON thin films," *J. Power Sources*, vol. 126, no. 1–2, pp. 134–138, 2004, doi: 10.1016/j.jpowsour.2003.08.030.

[56] T. Takahashi, K. Kuwabara, and M. Shibata, "Solid-state ionics - conductivities of Na+ ion conductors based on NASICON," *Solid State Ionics*, vol. 1, no. 3–4, pp. 163–175, 1980, doi: 10.1016/0167-2738(80)90001-6.

[57] S. Naqash, Q. Ma, F. Tietz, and O. Guillon, "Na3Zr2(SiO4)2(PO4) prepared by a solution-assisted solid state reaction," *Solid State Ionics*, vol. 302, pp. 83–91, 2017, doi: 10.1016/j.ssi.2016.11.004.

[58] B. Yan *et al.*, "NASICON-structured solid-state electrolyte Li 1.5 Al 0.5-x Ga x Ge 1.5 (PO 4) 3 prepared by microwave sintering," *Mater. Technol.*, vol. 34, no. 6, pp. 356–360, 2019, doi: 10.1080/10667857.2018.1563964.

[59] M. Monchak *et al.*, "Lithium Diffusion Pathway in Li1.3Al0.3Ti1.7(PO4)3 (LATP) Superionic Conductor," *Inorg. Chem.*, vol. 55, no. 6, pp. 2941–2945, 2016, doi: 10.1021/acs.inorgchem.5b02821.

[60] V. Epp, Q. Ma, E. M. Hammer, F. Tietz, and M. Wilkening, "Very fast bulk Li ion diffusivity in crystalline Li1.5Al0.5Ti1.5(PO4)3 as seen using NMR relaxometry," *Phys. Chem. Chem. Phys.*, vol. 17, no. 48, pp. 32115–32121, 2015, doi: 10.1039/c5cp05337d.

[61] Z. Kou, C. Miao, Z. Wang, and W. Xiao, "Novel NASICON-type structural Li1.3Al0.3Ti1.7SixP5(3-0.8x)O12 solid electrolytes with improved ionic conductivity for lithium ion batteries," *Solid State Ionics*, vol. 343, no. August, p.

115090, 2019, doi: 10.1016/j.ssi.2019.115090.

[62] M. Weiss, D. A. Weber, A. Senyshyn, J. Janek, and W. G. Zeier, "Correlating Transport and Structural Properties in Li1+ xAlxGe2- x(PO4)3 (LAGP) Prepared from Aqueous Solution," *ACS Appl. Mater. Interfaces*, vol. 10, no. 13, pp. 10935–10944, 2018, doi: 10.1021/acsami.8b00842.

[63] Q. Liu *et al.*, "Self-Healing Janus Interfaces for High-Performance LAGP-Based Lithium Metal Batteries," *ACS Energy Lett.*, vol. 5, no. 5, pp. 1456–1464, 2020, doi: 10.1021/acsenergylett.0c00542.

[64] Q. Liu *et al.*, "Safe LAGP-based all solid-state Li metal batteries with plastic super-conductive interlayer enabled by in-situ solidification," *Energy Storage Mater.*, vol. 25, no. September 2019, pp. 613–620, 2020, doi: 10.1016/j.ensm.2019.09.023.

[65] Q. Guo *et al.*, "New Class of LAGP-Based Solid Polymer Composite Electrolyte for Efficient and Safe Solid-State Lithium Batteries," *ACS Appl. Mater. Interfaces*, vol. 9, no. 48, pp. 41837–41844, 2017, doi: 10.1021/acsami.7b12092.

Chapter 3: Review on Experimental and Characterization Techniques

3.1 Synthesis Technique

There are a number of different approaches that may be used in order to successfully produce the electrolyte material in the laboratory. Some of these techniques need for specialized tools, while others may be carried out without the use of any additional supplies. The selection of the synthesis method that will be used to produce mostly depends on the desired size, the acceptable qualities of the surface, and the kind of material that is being worked with, such as semiconductors, metals, polymers, ceramics, and so on. The yield of SSEs has been enhanced via research and development of these processes in order to acquire better structural characteristics and higher levels of purity. Some of these techniques are given below:

3.1.1 Solid state method

The solid state approach is characterized by large-scale production and low cost at room temperature and ambient pressure. Additionally, the synthesis procedure for this technique is quite straightforward. Additionally, the size may be decreased, and homogenous nanomaterials can be produced in huge quantities in a very short length of time. Finely ground powders may be found during the manufacturing process of SSEs. These powders not only have strong interfacial contact, but they also possess uniformity in phases and can be sintered at low temperatures [1]. Experiments showed that the grain resistance of ternary composites samples did not change as a result of using this synthesis process. On the other hand, the activation energy was found to have lowered, and the grain boundary resistance was shown to have been changed. The synthesis of ternary composites was accomplished by a mechanical activation approach that was aided by the addition of lithium fluoride (LiF). The synthesis of ternary composites, sintered at 900℃ for 4 hours did not need any prior assistance, and it likewise generated good electrochemical performance. The creation of cracks, holes, and voids as a consequence of using this approach is the primary drawback. These features restrict the routes at grain boundaries,

which leads to poor performance of the SSE.

Following steps involve in solid state method:

- Appropriate material selection
- Mixing of materials
- Calcination
- Formation of pellets
- Sintering
- Characterization

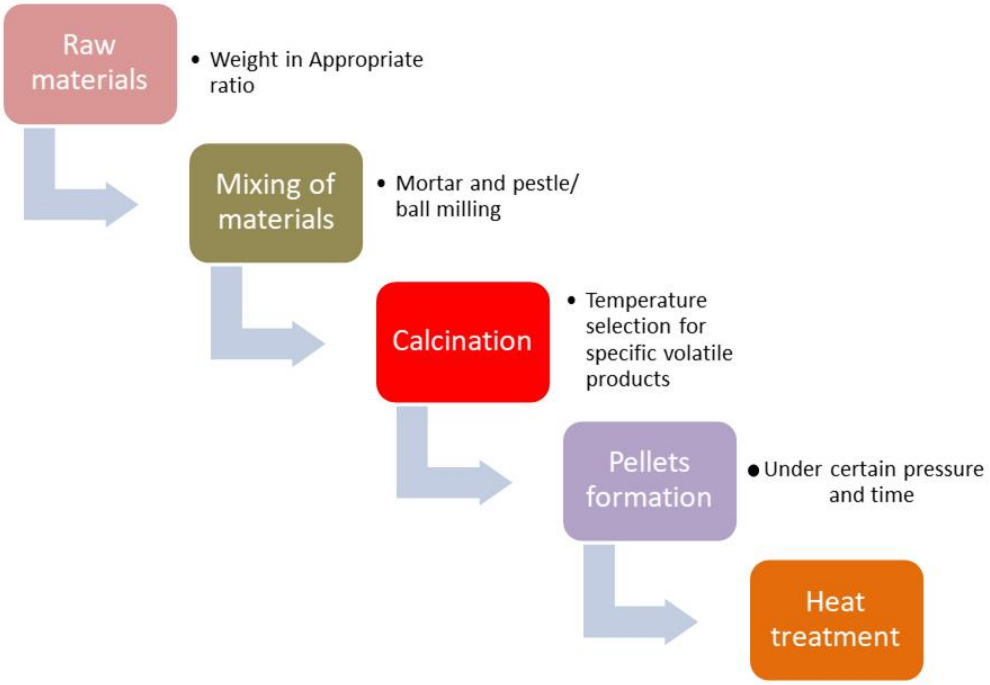

Figure 3-1. Solid state synthesis method

3.1.1.1 Appropriate material selection

In order to increase the surface area for interaction between particles, the materials that are often used take the form of fine powder. These components should not be inert and should instead have a high level of reactivity. The composition need to be well determined right from the beginning. Typically, lithium carbonate Li_2CO_3, aluminum oxide Al_2O_3,

silicon dioxide SiO_2, and ammonium dihydrogen phosphate $NH_4H_2PO_4$ are the starting materials for composite based solid state electrolytes [2].

3.1.1.2 Mixing of materials

The mixing of materials done by using mortar and pestle for 30 minutes. After that planetary ball milling is used for fine power.

3.1.1.3 Calcination

In order to give heat treatment to staring material for evaporation of unnecessary products from the material. In the ternary composites to decompose NH_4 from ammonium dihydrogen phosphate $NH_4H_2PO_4$, CO_2 and H_2O.

3.1.1.4 Formation of pellets

A specific pressure is used to form the pellets in order to maximize the contact between the reagents and reduce the contact with the sample crucible. Pellets may be held together in pellet shape by an organic binder [3].

3.1.1.5 Sintering

The sample is sintered at a certain temperature in order to react with the oxide and produce the desired product. The Tamman's rule and the volatilization potential influence the temperature selection. In accordance with Tamman's rule, the reaction can't begin until one of the reagents has reached a melting point that is two-thirds of its melting point. As a result, the reaction's environment is crucial [4].

3.2 Characterization techniques

3.2.1 Thermo-Gravimetric Analysis (TGA)

Instruments used for thermogravimetric analysis (TGA) include the thermogravimetric analyzer. The three basic thermogravimetric measurements of mass, temperature, and time may be used to produce a plethora of other metrics. Temperature-dependent thermal analysis (TGA) is a technique of thermal analysis in which a sample's mass is determined over a period of time as the temperature varies. Additionally, this measurement offers information on physical and chemical processes including thermal breakdown as well as solid-gas interactions like adsorption and desorption (e.g., oxidation or reduction) [5].

Thermogravimetric analysis (TGA) determines weight losses in a material with a change in temperature in a controlled atmosphere. The major applications of this characterization technique are the measurement of thermal stability, volatile content, moisture, organic linker in a sample, and the percent composition of components in a compound. The principle is that the temperature is gradually increased from zero to the required final temperature in a specific gas atmosphere which maybe Ar, air or some other gas. Now when temperature increases the contents in the sample start to evaporate. Moisture is usually the first content that removes from the sample so a change in mass of sample occurs. This mass is measured on the weight balance continuously during the process which is placed outside the furnace Figure 3.2. After moisture other volatile contents like organic residues start to escape. The stability of the sample can be defined as the temperature at which the material starts to decompose which is the main point in the curve. After that the line drops sharply causing a major loss in material [6]. This point is called the decomposition temperature and determines the stability of material. The weight of the material is mapped against temperature or time to demonstrate the thermal changes in the sample, for instance, the loss of solvent, loss of water of hydration, and the decomposition of the material. At the end of the process, the final mass residue is noted, and the total mass loss is calculated [7].

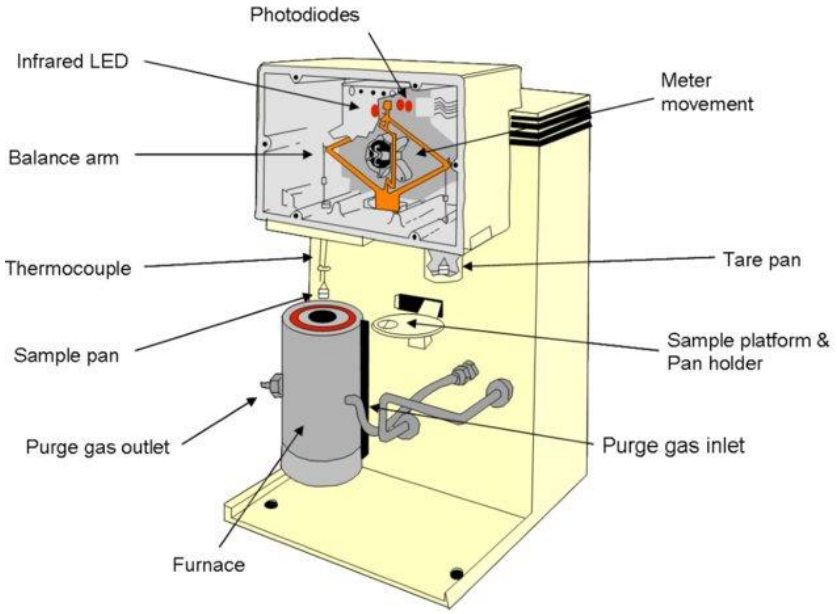

Figure 3-2. Schematic of TGA [7].

3.2.2 X-ray Diffraction (XRD)

Diffraction is the scattering of electromagnetic waves by a periodic long-range array, resulting in constructive interference at certain angles. When the electromagnetic waves involved are X-rays, it is termed as X-ray diffraction (XRD) [8].

It was Von Laue in 1912, who suggested that crystals may be possibly used as diffraction gratings for X-rays. X-rays due to their wavelength (λ) resemblance with the distance between crystal atoms are considered suitable for diffraction by crystals. X-ray diffraction in crystals is a combination of two processes, i.e., scattering of X-rays by individual atoms and interference of the scattered X-rays. The following few lines explain this concept [9].

Each atom is a coherent scattering point, as its electrons do. An atom's light scattering strength is determined by its electron count. Crystals may diffract X-rays due to their periodic array of long-range organized atoms. The X-rays dispersed by atoms in a substance reveal their atomic organization. Amorphous materials lack periodicity and consequently lack a distinctive diffraction pattern. Thus, the diffraction pattern is indicative of a material's unique microstructure. A pattern is predicted for various atom arrangements. Many peaks may be seen in a single diffraction pattern of material [10].

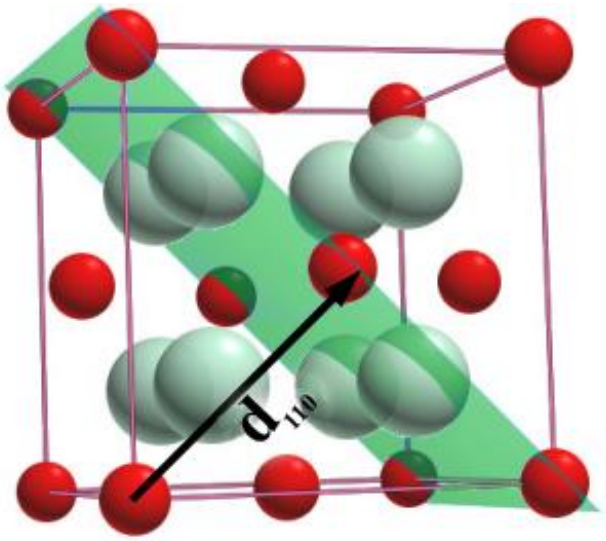

Figure 3-3. The position of the diffraction peaks is determined by the distance (d) between parallel atomic planes [11].

A crystal's structure is defined by its unit cell, whereas a crystal system describes the shape of the unit cell. Different planes of atoms are identified by Miller indices (hkl). The different diffraction peaks, that are commonly observed in the diffraction pattern of a single material, can be correlated to these atomic planes. Figure 3.4 explains the concept of different atomic planes and thus the different positions of peaks in a diffraction pattern.

Figure 3-4. X-ray Diffraction (D8-ADVANCE).

Bragg's law, in this regard, relates the angle for constructive interference with the interplane spacing. It states that for X-rays of wavelength λ falling on a family of parallel atomic planes, constructive interference occurs only at a specific angle 2θ.

$$\boldsymbol{n\lambda = 2d_{hkl} \sin \theta} \qquad (3.1)$$

Here, n is a positive integer, whereas d_{hkl} indicates the magnitude of the vector starting from the origin of the unit cell to the plane (hkl). In simple words, it indicates the interplane distance between two adjacent planes of the (hkl) family.

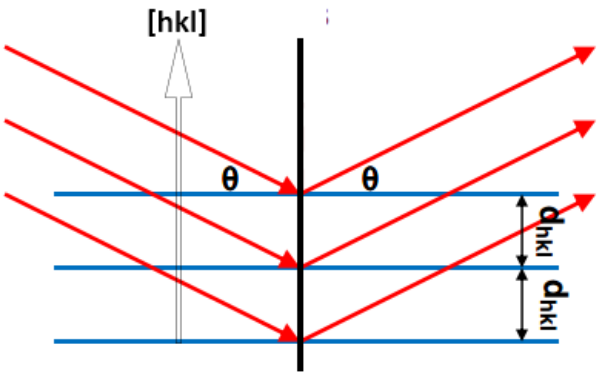

Figure 3-5. Scattering of X-rays of same λ and phase after falling on a crystal of interplane spacing, d_hkl at an angle θ [12].

3.2.3 Scanning Electron Microscopy

Scanning electron microscopy (SEM) involves the interaction between highly energetic electrons in the form of a focused beam, and a sample surface to produce several signals containing information about the sample. These signals contain valuable information regarding the morphology, topography, composition, microstructure, and material orientation of the test sample. Selected areas, as well as selected points, could be analyzed with SEM [13].

The energy of the fast-moving electrons is converted into other forms upon interaction with the sample. Some very useful signals are produced because of the electrons striking against the sample surface, including secondary electrons (SeE), backscattered electrons (BSE), diffracted BSE, X-rays, visible light, and heat. SeE and BSE are used for imaging purposes. SeE is especially important for morphology imaging and topography. BSE are often employed for showing compositional contrasts to distinguish phases from each other. Characteristic X-rays contain information on the chemical composition of the material [14]. A scanning electron microscope typically requires an electron gun to eject electrons. The electron gun typically employs a tungsten filament, which upon heating thermionically emits electrons. A portion of the electrons, due to high velocities pass by the anode plate and stream down the column. In the process, the electrons acquire energy typically in the range 0.2 – 40 keV. The electrons are then focused by one or two lenses to a spot of diameter in the range 0.4 – 5 nm.

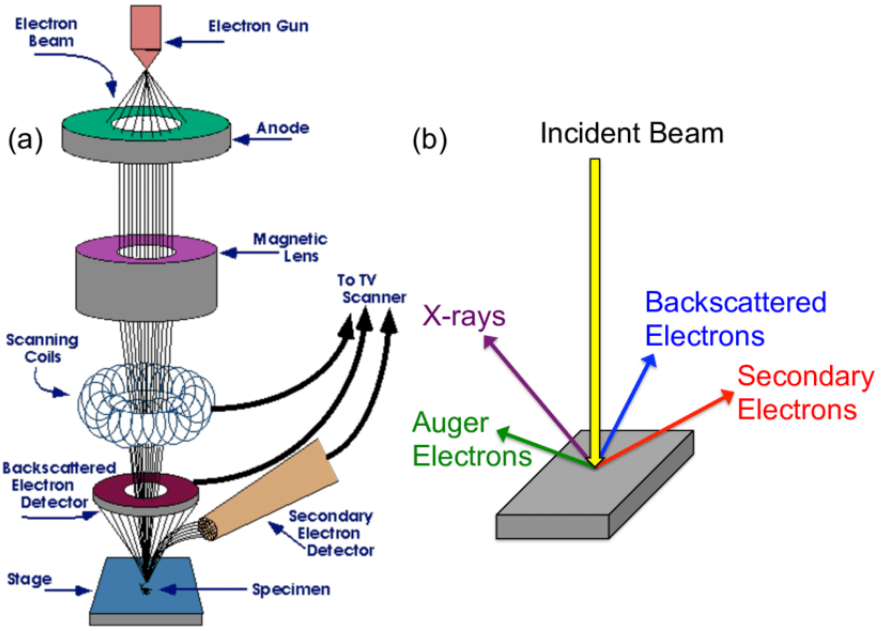

Figure 3-6. Schematic of Scanning electron Microscopy [14].

This is followed by the passages of the beam through a pair of scanning coils or deflector plates. Here the beam is deflected in the xy-plane to cause a raster scan of the sample. The electrons lose energy because of interaction with the sample, resulting in several signals. Signal detectors in combination with data manipulation systems are used to gather information of interest. The information is further sent to the display devices. The whole process takes place at reduced pressures since electron travel with least scattering requires vacuum conditions. Conventional SEM requires samples that are conductive and grounded to avoid charge buildup on the sample. Conductive samples such as metals don't require any special sample preparation procedures. Conductive samples may require cleaning followed by subsequent mounting onto the stub. However, insulating samples should be coated with a thin conducting material to avoid charge buildup on the specimen. Gold (Au) is often employed to deposit thin conducting film over non-conducting samples. Sample charging due to charge buildup results in image distortion and blurring since the incident electrons are repelled by this negative charge on the sample. For analyzing cross-section samples, cutting and polishing are often required. Cross-sections are usually mounted on a cross-section holder.

Figure 3-7. Scanning electron microscopy (TECASN Vega 3) [15].

Other than that, biological samples that are soft and contain fluids, to be analyzed by conventional SEM, require chemical fixation and dehydration prior to analysis [15].

In this work, Diamond like carbon film and Zinc Oxide thin film's morphology was analyzed by using VEGA 3 LMU, TESCAN model of SEM.

3.2.4 Energy Dispersive X-ray Spectroscopy

As seen in Figure 3-17, energy dispersive X-ray spectroscopy (EDS, EDX, XEDS, or EDXS), also referred to as energy dispersive X-ray microanalysis (EDXMA) or energy dispersive X-ray analysis (EDXA), is a method used to determine the elemental composition of a sample. EDS is predicated on the premise that each element is composed of atoms with a distinct atomic structure. Thus, each element emits a distinct collection of distinctive x-rays upon stimulation. To cause a sample to emit X-rays, the sample must be bombarded with a beam of energetic charged particles (electrons or protons), or X-rays. Thus, EDS entails the examination of the X-ray spectra produced by the bombardment in order to determine the elemental composition [16].

When particles/radiations fall on a surface, depending upon the energy of the falling particles/radiations and the binding energies of the electrons, electrons might be removed from the surface. Sufficiently energetic particles/radiations can even remove inner shell electrons from the sample atoms. When an inner shell electron is removed, a vacancy

(hole) is created in that shell. An electron from an outer orbit falls into that hole. This transition results in X-ray emission, characteristic of that element. X-ray lines are labeled by a capital letter that indicates the shell where the vacancy existed.

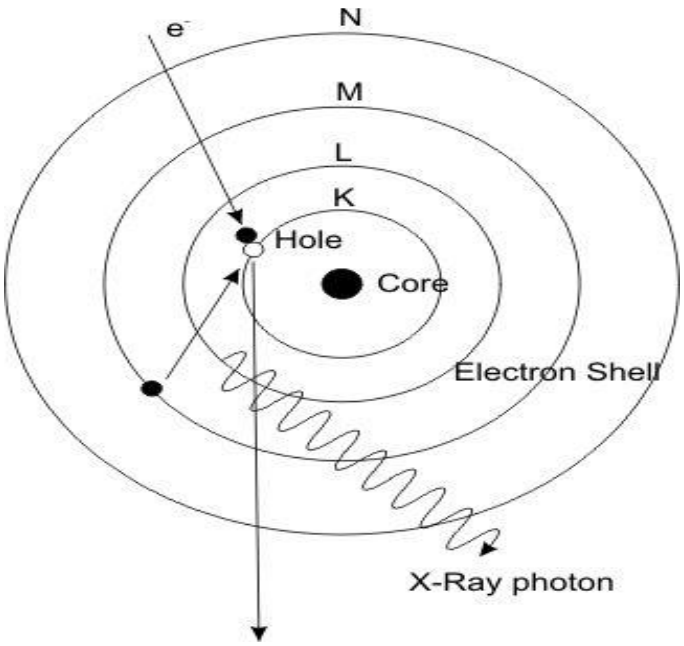

Figure 3-8. Working Principle of EDX [16].

It may be K, L, or M, followed by a Greek letter ($\alpha, \beta, etc.$). α lines are the most important ones, β lines are less important than α but more important than lines indicated by other Greek letters that follow, and so on. The Greek letter is followed by a number (1, 2, etc.) in subscript, that corresponds to the intensity of the line in that peculiar group, such as Kα_1. Among the numbers, 1 stands for maximum intensity, while others in the sequence represent a correspondingly decreasing intensity. When there is no number mentioned, it represents the combined intensity from all the X-rays in that group, such as Kα. Sometimes, the combined line is represented by mentioning more than one number in subscript, such as K$\alpha_{1,2}$ [17-18].

3.2.5 FTIR Spectroscopy

FTIR spectroscopy involves chemical bonds and functional groups identification because of IR absorption by the specimen. These absorptions can be associated with the stretching and bending of covalent bonds of molecules of a specimen. Stretching vibrations, which

are further classified as symmetric and asymmetric vibrations, are typically high energy vibrations than bending vibrations. It is to be noted that all covalent bonds are not capable of IR absorption. Only polar bonds are IR active and thus absorb IR radiations [19]. The results of IR spectroscopy are typically plotted as IR transmittance or absorbance vs IR frequency. Frequencies are represented as wavenumbers in units of cm^{-1}.

Figure 3-9. Fourier Transform Infrared Spectroscopy (Cary-630) [19].

The typical frequency range for IR spectroscopy is from 650 cm^{-1} to 4000 cm^{-1}. The intensity of the bands due to absorption in the transmittance or reflectance spectra depends on the dipole moment of the polar bond. For strong polar bonds, strong IR bands are observed. For medium polar bonds, medium intensity bands, whereas for weakly polar bonds, low-intensity bands are observed. For symmetric bonds, no bands are observable.

IR spectroscopy is useful for identifying molecular fragments such as functional groups, thus providing information on the molecular fingerprint of materials. IR spectroscopy, however, does not provide proof of chemical formula or structure.

Dispersive instruments have been traditionally applied for obtaining IR spectra. Prisms were used in the first dispersive IR instruments. Later, gratings replaced the prisms in these devices. A monochromator contains the prism/grating. the dispersive element disperses the energy entering through the entrance slit and reflects it towards the exit slit. At the exit slit, the spectrum is scanned before passing it forward to meet the detector.

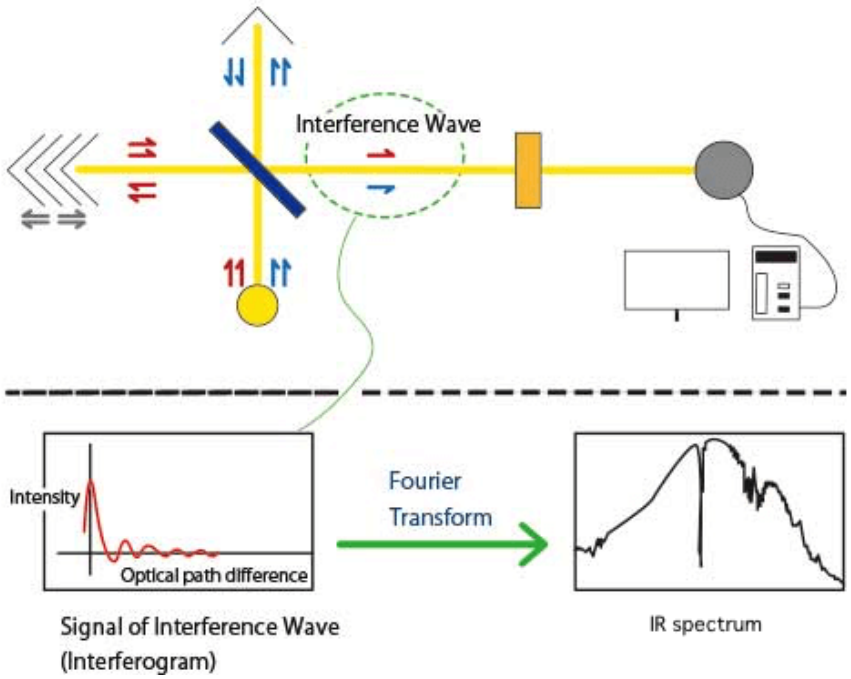

Figure 3-10. Schematic of FTIR spectroscopy [20].

Typically, the slit size of both the entrance and exit slits is programmed to vary to compensate for any variation of the input (source) energy with frequency. Thus, upon scanning the spectrum, the detector receives almost constant energy, provided no analysis sample is inserted. The monochromator in the dispersive IR spectrometer has certain

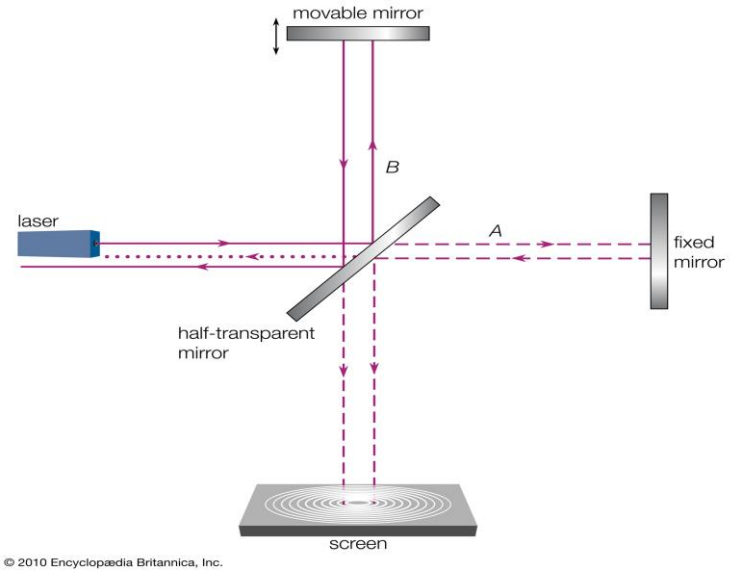

Figure 3-11. Schematic of a basic Michelson interferometer [20].

downsides. The entrance and the exit slits of the monochromator are meant to limit the frequency range of the energy to one resolution width. This makes the process too slow for a long-range of wavelengths. Samples that require quick speedy measurements, for example during online analysis, are not analyzable with such low sensitivity instruments.

During the 1970s, commercial IR instruments employing a very different method were introduced. These instruments quickly replaced the traditional dispersive instruments. Spectrometers today predominantly employ the Fourier transform method to obtain the IR spectra, hence the name Fourier transform infrared (FTIR) spectrometers. These devices are superior in performance as well as data handling capability [21].

Any sample in any state may be analyzed with FTIR spectroscopy. Gases, liquids, pastes, powders, solutions, films, fibers, and surfaces are all examinable with FTIR, provided a judicious sample preparation choice is made. There are three basic sample preparation techniques, which include;

Mix the sample with a mulling agent (mineral oil etc.) and press between NaCl plates. NaCl is used because it is cheap and it capable of avoiding IR absorptions up to the 650 cm^{-1} mark. However, below 650 cm^{-1}, NaCl plates become absorbing as well. On the other hand, KBr plates, which are costlier than NaCl, remain transparent to 400 cm^{-1} point. Although the salt may be IR transparent, the mineral oil used is an IR absorber, and that's the downside of this technique [22].

KBr Method

The second technique is the KBr method, which involves mixing the sample with KBr and making pellets of the mixture through high-pressure pressing. The mulling agent and hence the absorptions associated with the mulling agent are avoided in this case. Only solids could be analyzed with this technique and that's the limitation of this method [23].

Another method uses CCl_4 to dissolve the sample and then press it between the salt plates. CCl_4 in this case is an IR absorber that's the limitation of this method.

In the current study, we have employed FTIR spectroscopy to detect the hydrogenated carbon bonds on the surface of the substrates to confirm the presence of DLC film. Due to this fact, (Agilent Cary 630) was used to detection of antisymmetric bonds.

3.2.6 Raman Spectroscopy

Raman spectroscopy is a non-destructive system used to determine the chemical, structural, molecular interactions, polymorphism, and crystallinity of substances. It is entirely dependent on light's interaction with matter and on matter's interaction with itself. (Internal Chemical Bonds) The study of molecules is carried out using light scattering methods such as Raman. In this method, the molecules scatter light emitted by a high-intensity laser source. Rayleigh Scattered is so named because the majority of scattering light has the same wavelength (or colour) as the laser source and so provides no useful information. While a little amount of light is scattered at different wavelengths, the wavelengths at which light is dispersed change according to the chemical structure of the analyte; this is referred to as Raman Scattering [24].

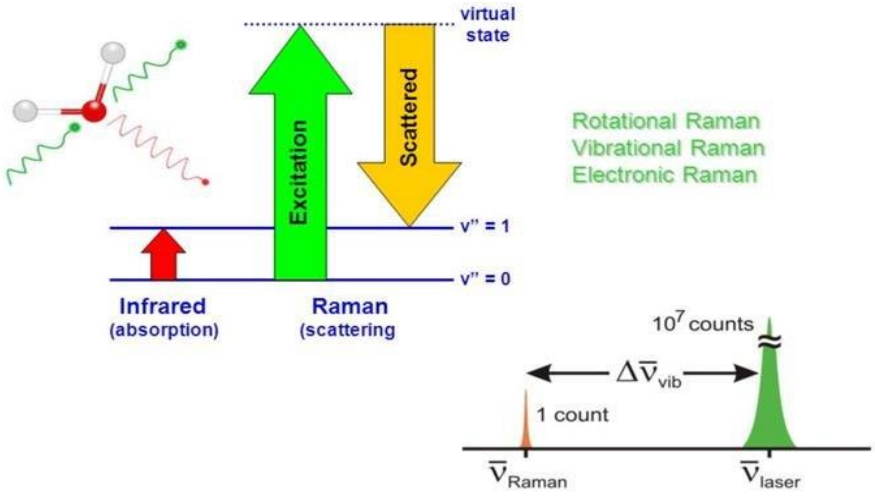

Figure 3-12. Working Principle of Raman Spectroscopy [24].

In a Raman spectrum, there are multiple peaks, each of which corresponds to a different intensity and spectrum position of the Raman scattered light. A separate chemical bond vibration is represented by each peak, including individual bonds such as C-C, C=C, N-O, and C-H, and groups of bonds.

3.2.7 Electrochemical Impedance Spectroscopy (EIS)

This technique of electrochemical workstation allows us to measure the resistivity of our system. This includes resistance of electrolyte, ohmic loss and or activation losses. Electrical resistance is the measure of the circuit element that resists the flow of current.

$$R = V/I \qquad (3.1)$$

According to Ohm's law, R is the resistance which is defined as the ratio of voltage (V), and current (I)[24]. This known law use is limited to only one circuit element, the ideal resistor.

An ideal resistor has several simplifying properties:

- The voltage passing through a resistor and the AC current are in a single phase.
- Ohm's Law is followed at every range of current and voltage.
- Resistance is not dependent on the frequency.

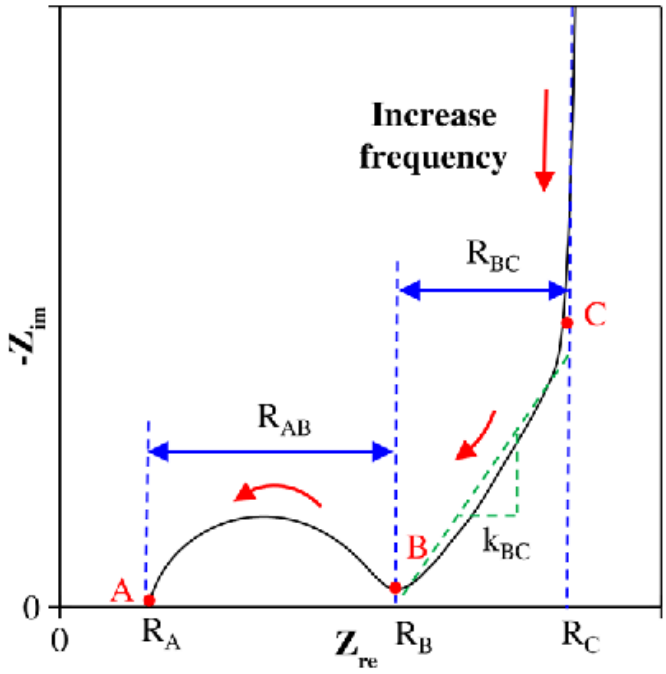

Figure 3-13. EIS Profile (Nyquist Plot) [25].

3.2.7.1 Electrochemical Parameters

The determination of the ionic conductivity is crucial to evaluate the efficiency of ASSLBs. EIS technique is used to measure the grain conductivity and total ionic conductivity of a solid electrolyte: The total ionic conductivity can be determined using:

$$\sigma = \frac{4t}{\pi d^2 R} \tag{3.3}$$

Where, σ, t, d, and R represent the ionic conductivity, thickness, diameter of the pellets, and total resistance. It is the sum of grain resistance and grain boundary resistance or charge transfer resistance [26].

Summary

This chapter initially discusses different chemical synthesis methods like solid state method. After that material characterization techniques have been studied i.e., TGA, XRD, SEM, EDS, FTIR, Raman and EIS. Main principle of these techniques has been noted down along with diagrams. After that the whole electrochemical testing process implemented was explained and electrochemical performance determination using EIS with a four-electrode system.

References

[1] T. Takahashi, K. Kuwabara, and M. Shibata, "Solid-state ionics - conductivities of Na+ ion conductors based on NASICON," *Solid State Ionics*, vol. 1, no. 3–4, pp. 163–175, 1980, doi: 10.1016/0167-2738(80)90001-6.

[2] N. S. Mohamed, R. H. Y. Subban, and R. Rusdi, "Enhancement of electrical properties of NASICON-type solid electrolytes (LiSn2P3O12) via aluminium substitution," *J. Sci. Adv. Mater. Devices*, vol. 5, no. 3, pp. 368–377, 2020, doi: 10.1016/j.jsamd.2020.06.003.

[3] F. Zheng, M. Kotobuki, S. Song, M. O. Lai, and L. Lu, "Review on solid electrolytes for all-solid-state lithium-ion batteries," *J. Power Sources*, vol. 389, no. April, pp. 198–213, 2018, doi: 10.1016/j.jpowsour.2018.04.022.

[4] C.J.Brinker;G.W.Scherer,"Sol-Gel_Science_The_physics_and_chemistry_of_sol-gel_processing_-_Brinker_1990.pdf." p. 462, 1990. doi: 10.1016/S0254-0584(02)00315-2.

[5] S. D. Lee *et al.*, "Composite Electrolyte for All-Solid-State Lithium Batteries: Low-Temperature Fabrication and Conductivity Enhancement," *ChemSusChem*, vol. 10, no. 10, pp. 2175–2181, 2017, doi: 10.1002/cssc.201700104.

[6] J. Lai, W. Niu, R. Luque, and G. Xu, "Solvothermal synthesis of metal nanocrystals and their applications," *Nano Today*, vol. 10, no. 2, pp. 240–267, 2015, doi: 10.1016/j.nantod.2015.03.001.

[7] X. Dong, M. Qi, Y. Tong, and F. Ye, "Solvothermal synthesis of single-crystalline hexagonal cobalt nanofibers with high coercivity," *Mater. Lett.*, vol. 128, pp. 39–41, 2014, doi: 10.1016/j.matlet.2014.04.133.

[8] S. Sōmiya and R. Roy, "Hydrothermal synthesis of fine oxide powders," *Bull. Mater. Sci.*, vol. 23, no. 6, pp. 453–460, 2000, doi: 10.1007/BF02903883.

[9] S. Feng and R. Xu, "New materials in hydrothermal synthesis," *Acc. Chem. Res.*, vol. 34, no. 3, pp. 239–247, 2001, doi: 10.1021/ar0000105.

[10] H. Khan, A. S. Yerramilli, A. D'Oliveira, T. L. Alford, D. C. Boffito, and G. S.

Patience, “Experimental methods in chemical engineering: X-ray diffraction spectroscopy—XRD,” *Can. J. Chem. Eng.*, vol. 98, no. 6, pp. 1255–1266, 2020, doi: 10.1002/cjce.23747.

[11] M. Y. A. Mollah, F. Lu, and D. L. Cocke, “An X-ray diffraction (XRD) and Fourier transform infrared spectroscopic (FT-IR) characterization of the speciation of arsenic (V) in Portland cement type-V,” *Sci. Total Environ.*, vol. 224, no. 1–3, pp. 57–68, 1998, doi: 10.1016/S0048-9697(98)00318-0.

[12] J. Kacher, C. Landon, B. L. Adams, and D. Fullwood, “Bragg’s Law diffraction simulations for electron backscatter diffraction analysis,” *Ultramicroscopy*, vol. 109, no. 9, pp. 1148–1156, 2009, doi: 10.1016/j.ultramic.2009.04.007.

[13] Y. Leng, *Materials characterization: Introduction to microscopic and spectroscopic methods: Second edition*. 2013. doi: 10.1002/9783527670772.

[14] W. Zhou, R. Apkarian, Z. L. Wang, and D. Joy, “Fundamentals of scanning electron microscopy (SEM),” *Scanning Microsc. Nanotechnol. Tech. Appl.*, pp. 1–40, 2007, doi: 10.1007/978-0-387-39620-0_1.

[15] K. D. Parry V, “Microscopy : An introduction,” *III-Vs Rev.*, vol. 13, no. 4, pp. 40–44, 2000.

[16] L. J. Allen, A. J. D’Alfonso, B. Freitag, and D. O. Klenov, “Chemical mapping at atomic resolution using energy-dispersive X-ray spectroscopy,” *MRS Bull.*, vol. 37, no. 1, pp. 47–52, 2012, doi: 10.1557/mrs.2011.331.

[17] D. E. Newbury and N. W. M. Ritchie, “Is scanning electron microscopy/energy dispersive X-ray spectrometry (SEM/EDS) quantitative?,” *Scanning*, vol. 35, no. 3, pp. 141–168, 2013, doi: 10.1002/sca.21041.

[18] T. C. Lovejoy *et al.*, “Single atom identification by energy dispersive x-ray spectroscopy,” *Appl. Phys. Lett.*, vol. 100, no. 15, 2012, doi: 10.1063/1.3701598.

[19] B. A. Boukamp, “Fourier transform distribution function of relaxation times; application and limitations,” *Electrochim. Acta*, vol. 154, pp. 35–46, 2015, doi: 10.1016/j.electacta.2014.12.059.

[20] C. Berthomieu and R. Hienerwadel, “Fourier transform infrared (FTIR) spectroscopy,” *Photosynth. Res.*, vol. 101, no. 2–3, pp. 157–170, 2009, doi: 10.1007/s11120-009-9439-x.

[21] J. M. Hollander, W. L. Jolly, and J. M. Hollander, “X-Ray Photoelectron Spectroscopy,” vol. 17, no. June, pp. 193–200, 1970.

[22] C. S. Fadley, “X-ray photoelectron spectroscopy: Progress and perspectives,” *J. Electron Spectros. Relat. Phenomena*, vol. 178–179, no. C, pp. 2–32, 2010, doi: 10.1016/j.elspec.2010.01.006.

[23] A. Proctor and P. M. A. Sherwood, “Data Analysis Techniques in X-ray Photoelectron Spectroscopy,” *Anal. Chem.*, vol. 54, no. 1, pp. 13–19, 1982, doi: 10.1021/ac00238a008.

[24] D. D. MacDonald, “Reflections on the history of electrochemical impedance spectroscopy,” *Electrochim. Acta*, vol. 51, no. 8–9, pp. 1376–1388, 2006, doi: 10.1016/j.electacta.2005.02.107.

[25] B. A. Mei, O. Munteshari, J. Lau, B. Dunn, and L. Pilon, “Physical Interpretations of Nyquist Plots for EDLC Electrodes and Devices,” *J. Phys. Chem. C*, vol. 122, no. 1, pp. 194–206, 2018, doi: 10.1021/acs.jpcc.7b10582.

[26] J. Huang, Z. Li, B. Y. Liaw, and J. Zhang, “Graphical analysis of electrochemical impedance spectroscopy data in Bode and Nyquist representations,” *J. Power Sources*, vol. 309, pp. 82–98, 2016, doi: 10.1016/j.jpowsour.2016.01.073.

Chapter 4: Methodology and Experimentation

4.1 Material procurement

The analytical pure of all starting materials were acquired from Sigma Aldrich. Ternary composite, Mn-ternary composite, and Co-ternary composite are synthesized using lithium carbonate (Li_2CO_3, ≥99.0%), aluminum oxide (Al_2O_3, 99.99%), silicon dioxide (SiO_2, ~99.0%), and ammonium dihydrogen phosphate ($NH_4H_2PO_4$, 98 atom%). Dopants were comprised manganese nitrate hydrate ($Mn(NO_3)_2 \cdot xH_2O$, 98.0%) and cobalt nitrate hexahydrate ($Co(NO_3)_2 \cdot 6H_2O$, 98.0%).

4.2 Material Synthesis

4.2.1 Synthesis of Ternary Composite

Ternary composite ($AlPO_4$-SiO_2-$Li_4P_2O_7$) solid electrolytes were synthesized by mixing 3.6857 g of Li_2CO_3, 1.7107 g of Al_2O_3, 3.0243 g of SiO_2, and 11.5794 g of $NH_4H_2PO_4$ as shown in Scheme 1. In an agate mortar and pestle, the powders were pounded and blended for 30 minutes. The material was mechanically activated by planetary ball milling apparatus (High-Speed Shimmy Ball Mill SFM-1 (QM-3SP2)) at 800 rpm for 3 hours with intervals to avoid heating of the apparatus and transferred to zirconium oxide grinding jars with rubber seals containing 5 ZrO_2 balls with a weight ratio of 1:20. The material was calcined in an alumina boat at 350 ℃ for 6 hours by keeping the ramp rate of 5 ℃/min in a box resistance furnace with constant air (Model: MTP-950-3-P). After allowing the mixture to cool to room temperature, it was pounded to a fine powder in a pestle and mortar for 20 minutes. Following that, pellets with a diameter of 10 mm were manufactured at a pressure of 10 MPa for 25 minutes. These pellets were sintered in a Magma box furnace at a temperature of 900 ℃ for 4 hours with a heating rate of 5 ℃ per minute in air. The samples were allowed to cool naturally to room temperature [1].

4.2.2 Synthesis of Mn-Ternary Composite and Co-Ternary Composite

The Co and Mn -ternary composite pellet was made by combining 3.5747 g of Li_2CO_3, 1.3273 g of Al_2O_3, 2.9332 g of SiO_2, 0.9342 g of Mn $(NO_3)_2.6H_2O$ and Co $(NO_3)_2.6H_2O$, and 11.2306 g of $NH_4H_2PO_4$ into a 20 g total material weight. The identical step-by-step

technique was followed for the synthesis of both Mn-ternary composite and Co-ternary composite, the sintering was done at just 900℃.

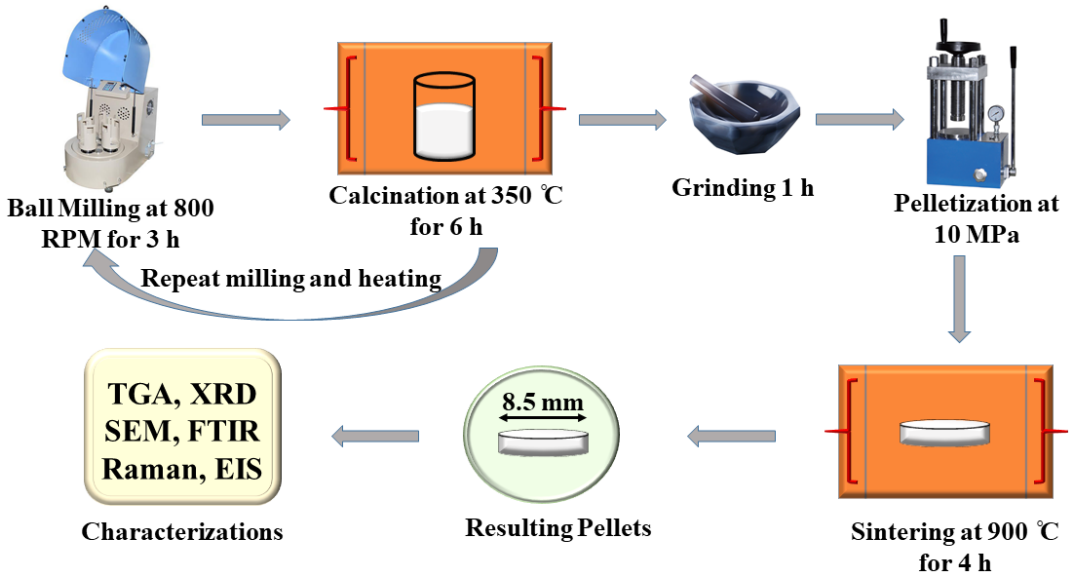

Figure 4-1. Synthesis of Ternary Composite-based solid-state electrolyte via solid-state reaction process.

4.3 Instruments and Material Characterization

The phase of the prepared samples were examined using a Bruker D8 Advance X-ray diffractometer with an LYNXEYE detector and Cu-k radiation. The measurements were made in the range of 10°–75° with a step of 0.02°. Scanning electron microscopy ((SEM), VEGA3, 51–ADD0007 Tescan, Brno, Czech Republic) was used to obtain the morphological analysis of the samples. Fourier transformed infra-red ((FTIR), Cary 630 FTIR spectrometer) spectra of the materials were acquired between 400 and 4000 cm^{-1} to study the antisymmetric bonding structure. To evaluate the structural characteristics of the ternary composite, the 532 nm wavelength Apollo Raman laser was utilized. Thermogravimetric analysis (TGA) was executed at a heating rate of 10 ℃/min in a temperature range of 25 ℃ to 800 ℃ to determine the weight loss of ternary composites. Before characterizing the pellet's AC impedance, thin gold (Au) films were deposited on both sides of the pallet. For deposition, the vacuum sputter coater was employed, and each side of the pellet was coated for around 15 minutes [2]. This gold layer serves as an ion-

blocking electrode. AC impedance measurements were conducted using a CHI660E potentiostat (Shanghai Chenhua Co., Ltd.) in a frequency range of 0.001–1MHz and an amplitude of 10 mV. Eq. 1 is used to compute the ionic conductivity, where σ, t, d, and R represent the ionic conductivity, thickness, diameter of the pellets, and total resistance. The overall resistance is equal to the summation of grain resistance and grain boundary resistance [3].

$$\sigma = \frac{4t}{\pi d^2 R} \tag{4.1}$$

Summary

The whole study of experimentation technique is described in detail in this chapter. It was explained in detail how ternary composite, Mn-ternary composite and Co-ternary composite were synthesized and characterized in the chapter. Finally, we have discussed the electrochemical testing method and parameters used on the electrochemical workstation.

References

[1] Y. Meesala *et al.*, “All-Solid-State Li-Ion Battery Using Li1.5Al0.5Ge1.5(PO4)3 As Electrolyte Without Polymer Interfacial Adhesion,” *J. Phys. Chem. C*, vol. 122, no. 26, pp. 14383–14389, Jul. 2018, doi: 10.1021/ACS.JPCC.8B03971.

[2] J. Guo, J. Zheng, W. Zhang, and Y. Lu, “Recent Advances of Composite Solid-State Electrolytes for Lithium-Based Batteries,” 2021, doi:10.1021/acs.energyfuels.1c01609.

[3] F. Ma *et al.*, “Preparation and evaluation of high lithium ion conductivity Li1.3Al0.3Ti1.7(PO4)3 solid electrolyte obtained using a new solution method,” *Solid State Ionics*, vol. 295, pp. 7–12, Nov. 2016, doi: 10.1016/J.SSI.2016.07.010.

Chapter 5: Results and Discussion

5.1 Material Characterization

5.1.1 TGA Analysis

As shown in Figure 1, the TGA curve of the novel oxide-based ternary composite ($AlPO_4$-SiO_2-$Li_4P_2O_7$) solid-state electrolyte for lithium batteries exhibits minimal weight loss of up to 22.26% in the region 25 °C to 900 °C due to degradation of volatile constituents including moisture, hydrates, carbonates and ammonia. Since most of the volatile components in the ternary composite sample had already evaporated during the calcination process. Other constituents, such as lithium oxide, aluminum phosphate, and amorphous silicate, have reached their evaporation points. Li_2O evaporation has previously been proven to cause the weight loss of the material LATP when heated to 1100 °C.

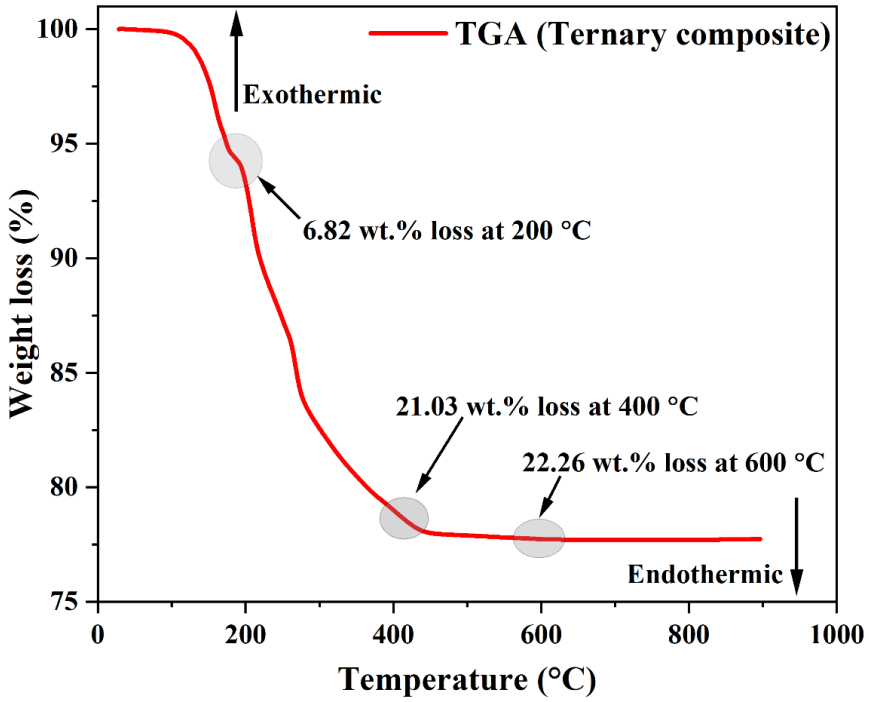

Figure 5-1. TGA and DSC spectra for ternary composite sample.

According to Antolini et al., the phase transition of the mixed oxide at approximately 950 °C has been used to determine a loss of blended $LiCO_2$ and lithium content [1]. These

observations were probably triggered by the evaporation of lithium oxide LiO. According to the findings of Brewer et al. and Kimura et al., the vapor pressure of Li_2O is greater than that of LiO, suggesting that Li_2O is evaporated at roughly 1100 °C [2,3]. The powder was prepared for a heating methodology based on the TGA findings, as indicated in the experimental setup.

5.1.2 X-Rays Diffraction

Figure 5-2, depicts the XRD patterns of the novel oxide-based ternary composite ($AlPO_4$-SiO_2-$Li_4P_2O_7$), Mn-ternary composite, and Co-ternary composite solid-state electrolyte sintered at a temperature of 900 ℃. The XRD spectrum of the ternary composite shows relection from $AlPO_4$ (JCPDS#48-0625) phase, which results in a detrimental influence on grain boundary conductivity [4]. This phase helps to improve the conductivity after the inclusion of dopants to this composite, which assists in the conduction of lithium ions into the solid electrolyte. The ternary phase also shows growth of another $Li_4P_2O_7$ (JCPDS#77-1045) phase [4]. The highest peak in XRD pattern of ternary composite correspond to the SiO_2 phase. Manganese and cobalt doping affect the intensity of $AlPO_4$ peaks. Manganese assists to improve the ionic conductivity after incorporation inside the composites. After manganese doping, the peak at 26.58° is relocated to a lower angle of 26.40°. The d-spacing is increased as a result of the implementation of manganese.

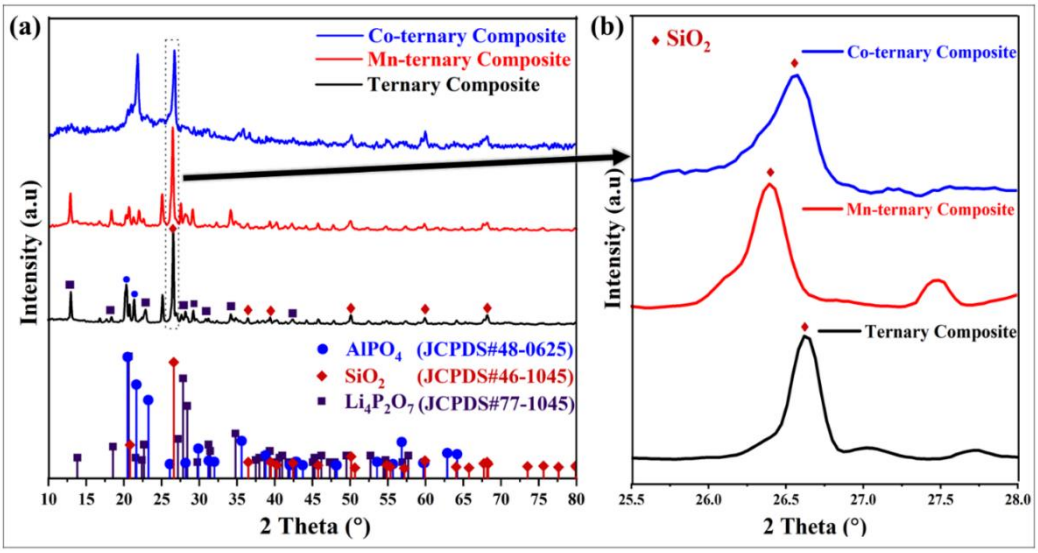

Figure 5-2. a) XRD spectra for ternary composite, Mn-ternary composite and Co-ternary composite b) High-resolution spectra for ternary composite, Mn-ternary composite, and Co-ternary composite for analyzing the shifting of peaks.

On the other hand, cobalt doping results in shift of 26.58° peak to higher angle of 26.61°, resulting in low d-spacing as shown in Figure 5-2 (b). The addition of the dopants will also affect the particle size and crystallite size of the base material [5]. Because of the size difference between the dopant and the host cations, the dopant is unable to completely enter the host structure. As a result of this size disparity, strain energy is generated, which pulls the host cation out of the lattice structure. These cations form oxide phases and segregate at grain boundaries that can be obstructing lithium-ion routes [6]. Furthermore, since it was created using solid-state technology, this material has a high degree of porosity. The small number of pores and cracks in the structure may assist in the efficient migration of Li ions through the framework.

5.1.3 SEM & EDX Analysis

Figure 5-3 (a)-(c) demonstrates the morphological and elemental composition analyses of ternary composites based on solid-state electrolytes using the SEM and energy dispersive X-rays (EDX) spectroscopy. The SEM image of ternary composite (Figure 5-3a) reveals that the particles are in micron size with agglamorated morpholgy. The particle size distribution of the ternary composites varied between 1.5 µm to 2.0 µm. The Mn-ternary composite reveals that the particles have flake-like assemblies (Figure 5-3b) with a size distribution in a range of 1.0 µm to 2.0 µm. The Co-ternary composite shows large particles with well-defined edges and the particle size distribution of 1.69 µm. The particle size was changed as a result of differences in the ionic radii of the dopant element and the host element after doping of Mn and Co inside the ternary composites [7].

Introducing dopants such as manganese and cobalt content inside the lattice structure of ternary composites results in a reduction in the particle size of the synthesized ternary composite's particles. This could be happened due to the inhibition of the Mn and Co cation to the crystal growth of base material. Additionally, Mn-ternary composites have a homogenous and dense structure. Mn-ternary composites have a more compact and homogenous crystalline structure. In comparison to the base sternary composite and Co-ternary composite, the Mn-ternary composite’s sample has the smallest crystallite size. This finding is very consistent with earlier conductivity study results [8], which indicate that Mn-ternary composite has the greatest conductivity. A higher conductivity is associated with smaller crystallite sizes, as demonstrated by Kumar et al. and Fuentes et

al. As per the author, ions are more easily channeled towards the electrodes in tiny crystallites than in bigger ones [9,10].

As indicated in Table 5-1, the elements like oxygen and phosphorus remained distributed consistently across the samples, however, the Al-rich zone (which does not include silicon) may be ascribed to the $AlPO_4$ phase, which results in agglomeration of the particles [11]. $AlPO_4$ demonstrates the presence of phase, which was mostly concentrated in the area of grain boundaries, which is consistent with the findings of Yu et al [12]. The compaction density may rise as a consequence of the doping of manganese and cobalt, which will result in an improvement in the performance of all-solid-state LIBs. The secondary phases are represented by the small crystals on the surface; when dopants such as manganese and cobalt are introduced into the base material of ternary composites, the impurity phases decrease and the lithium conducting passage is improved, increasing grain boundary conductivity.

According to the researchers, a ceramics-based solid-state electrolyte that was synthesized at a high sintering temperature (> 800 ^{o}C) triggered neck growth formation, in which the grains or particles were associated with one another. A reduction in pores and cracks as a consequence of the aggregation and proliferation of irregular particles has occurred, while the densification of the compounds has been increased [6].

Figure 5-3 a(ii), b(ii), c(ii) shows the EDX spectra of crystallized specimens that show that the elements Al, Si, P, O, Mn, and Co are present. It can be observed that all of the elements are consistently distributed in ternary composite-based ceramic materials, suggesting that Mn and Co have been effectively doped inside the base structure of the ternary composite. Due to the concept of charge neutrality, EDX is unable to determine lithium's wt.% and at.% [13]. As a result of these findings, the structural stability of the solid-state electrolyte utilized in all-solid-state cells throughout the charging and discharging cycles may be improved, which in turn helps to improve the battery's performance.s

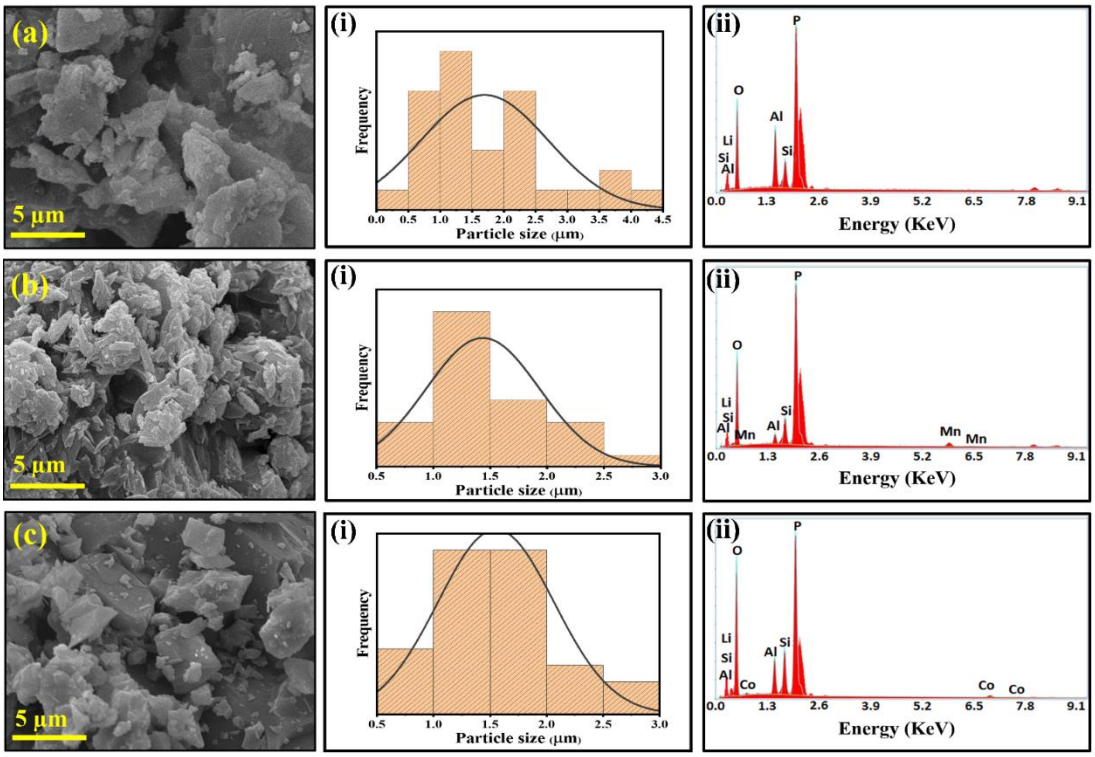

Figure 5-3. SEM images at 5 µm of the resolution, (a) Ternary composite, (b) Mn-ternary composites, (c) Co-ternary composites, (a)(i) Particle size distribution of Ternary composite, (b)(i) Particle size distribution of Mn-ternary composite, (c)(i) Particle size distribution of Co-ternary composite, (a)(ii) EDX spectra of ternary composite, (b)(ii) EDX spectra of Mn- ternary composite, (c)(ii) EDX spectra of Co-ternary composite.

Table 5-1. Elemental composition of Ternary composites, Mn- ternary composites, and Co-ternary composites.

Sample ID	**Atomic concentration (%)**							**Weight Concentration (%)**						
	Li	**Al**	**Si**	**P**	**O**	**Mn**	**Co**	**Li**	**Al**	**Si**	**P**	**O**	**Mn**	**Co**
Ternary composite	-	6.9	3.5	24.9	50.4	-	-	-	9.5	5.0	39.4	41.1	-	-
Mn-ternary composite	-	1.5	3.6	26.8	55.4	1.2	-	-	2.1	5.0	41.4	44.3	3.3	-

Co-ternary composite	-	4.1	4.7	21.8	61.1	-	0.6	-	5.6	6.6	34.1	49.2	-	1.8

5.1.4 FTIR Analysis

The functional group and structural analysis of ternary composite, Mn- ternary composite, and Co-ternary composite were determined using FTIR spectra. FTIR measurements were conducted in the range from 500 cm^{-1} to 3500 cm^{-1}. Composites like $AlPO_4$ and $Li_4P_2O_7$ might pertain to the $(PO_4)^{-3}$ structural unit of a solid-state electrolyte based on ternary composite [14]. These bands are illustrated by the bending, antisymmetric, and symmetric stretching of the various $(PO_4)^{-3}$ structural units. The bands between 550 and 650 cm^{-1} are directly associated with the O-P-O asymmetric bending vibrational mode, which is observable in the infrared spectrum. The band at 1040 cm^{-1} is associated with the stretching of $(PO_4)^{-3}$ ions, whereas the band at 825 cm^{-1} is related to the vibrations of the O-P-O bond [15-17]. The vibration of the Al-O bond is attributable to the bands at 780 cm^{-1} and 990 cm^{-1}. Furthermore, the peak positioned between 1050 and 1200 cm^{-1} relates to the formation of Si-O-Si bonds [18].

The presence of bands associated with aluminum silicate at around 1006 cm^{-1} verifies the presence of aluminum doping on the silicon side. Some of the peaks have a low intensity of the $(PO_4)^{-3}$ structural unit which could be owing to the aluminum, manganese, cobalt doping, and influence of sintering temperature in the base structure. The presence of peaks at 688 cm^{-1} and 523 cm^{-1} validates the doping of cobalt and manganese inside the ternary composite based on the solid-state electrolyte's base structure. The doping of manganese and cobalt within the ternary composite has a substantial impact on the intensity of the secondary phase and desirable bands of composites such as $AlPO_4$ and SiO_2. These dopants contribute to the reduction of inferior phases that helps to improve the ionic conductivity of the ternary composite based on solid-state electrolyte for LIBs [13].

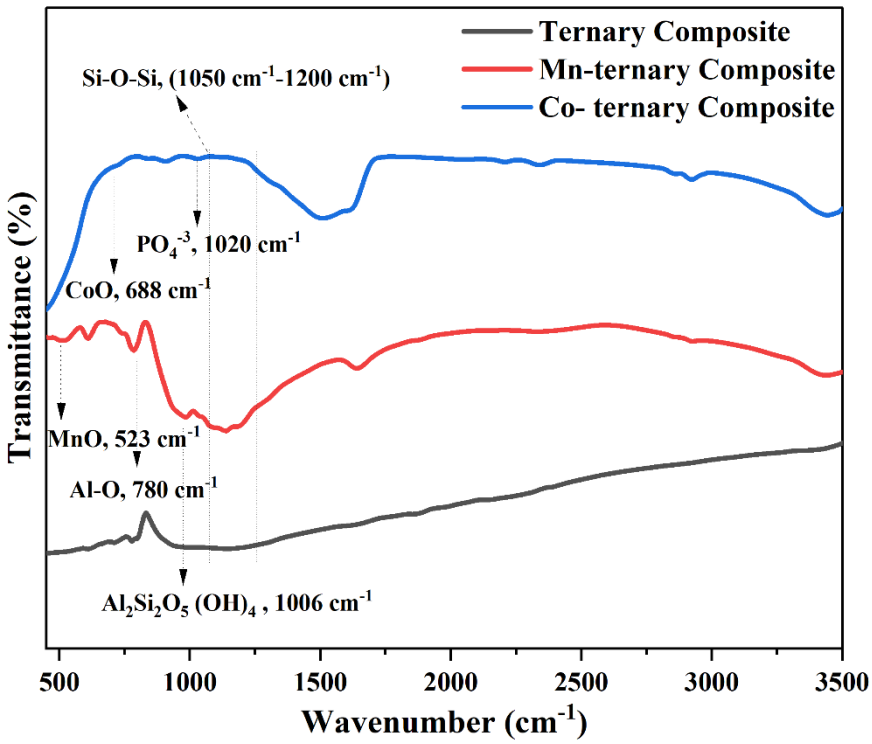

Figure 5-4. FTIR spectra for ternary composite, Mn-ternary composite, and Co-ternary composite based solid-state electrolyte.

5.1.5 Raman Spectroscopy

Raman spectroscopy is used for analyzing the structural characteristics of materials. The ability to discriminate between crystalline and amorphous phases using Raman spectroscopy makes this technique well-suited for studying amorphous auxiliary phases and assessing the information contained in composite materials. Another advantage of this characterization is spatial resolution in the ancillary phase distribution study, which is advantageous for evaluating the physical properties of ternary composite-based SSEs [19,20].

The Raman spectra were recorded to determine the local bonding structure of oxide-based ternary composite materials as shown in Figure 5-5. Since local bonding structuring has a considerable influence on the magnitude of the conduction route's local bottleneck, it is critical to integrate the idea of local bonding structure in ternary composite-based SSE systems [21]. Raman spectra of ternary composites, Mn-ternary composites, and Co-ternary composite materials were acquired in the 200 cm^{-1} to 1300 cm^{-1} range. The measured spectra show several broad band peaks, such as 200-500 cm^{-1}, 650-800 cm^{-1},

and 950-1150 cm^{-1}. These bands correspond to the antisymmetric, symmetric stretching, and bending of the various PO_4 structural units [22,23].

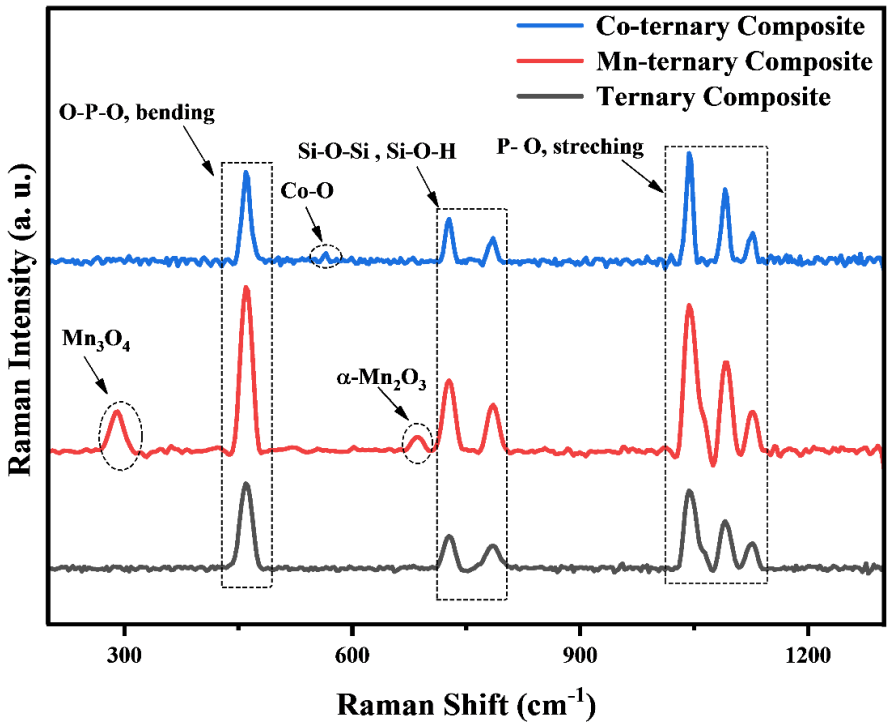

Figure 5-5. Raman Spectra for ternary composite, Mn-ternary composite, and Co-ternary composite based solid-state electrolyte.

Oxide-based solid-state electrolytes have the highest Raman scattering due to the apparent PO_4 structural units. These PO_4 groups are found to be interconnected between both the columns of SiO_x/AlO_x octahedra in ceramic-based materials, where they are observed to share the oxygen atoms with Si^{+4}/Al^{+3} and Li^+ ions present in the structure. The peaks at 291 cm^{-1} and near 690 cm^{-1} corresponds to the Mn_3O_4 and α-Mn_2O_3, respectively [24]. Similarly, the peak at 565 cm^{-1} correlated with Co-O [25]. This could be attributed to the successful doping of Mn and Co in the structure of ternary composite. The bands found in the spectra within the range of about 200 cm^{-1} to 500 cm^{-1} are associated with P-O-Al bending modes, while the bands detected within the range of 650-800 cm^{-1} are linked to asymmetric bending of a SiO_2 supporting structure. For amorphous silicate structural units, Si-O bending vibrations are identified around 730 cm^{-1}, whereas silica bending modes are detected at higher levels at 790 cm^{-1}. The significant levels of bending

frequencies are understandable since there is substantial clustering of oxygen due to the existence of octahedra groups, making amorphous silicate bending exceedingly difficult to achieve. The bands are observable above 900 cm^{-1} and are attributed to symmetrically stretched PO_4 tetrahedra. The vibrational functions of the phosphate group remain relatively robust. The subpeaks inside this zone indicate that the phosphate group's local structure has altered dramatically as a result of the clear aluminum substitution. The bands about 1043 cm^{-1} that are connected to the phosphate group are especially apparent since it has a higher stretch than $AlPO_4$ at approximately 1093 cm^{-1}. According to Barj et al., the broadening peak in the Raman spectra is induced by disordered PO_4 tetrahedra [26,27]. Due to the obvious proximity of the ionic radii of aluminum and silicon, the widening of the peaks can be explained by the formation of new Li-O bonds at the M_2 site, which must alter the P-O bonding and result in the widening of the Raman spectra in the Al substituted oxide-based solid electrolyte [21,28].

5.1.6 EIS Analysis

Figure 5-6 (a-c) illustrates the impedance spectra of ternary composite, Mn-ternary composite, and Co-ternary composite samples sintered at 900 ℃. The Au (gold) coating of sample pallet done for the current collection from EIS experimental setup. At high frequency, the impedance spectrum exhibits a semicircle, whereas, at low frequency, it exhibits an oblique line. The semicircle tends to come from the attributes of the grain boundaries, and the line indicates how lithium ions diffuse through the blocking Ag electrodes. Furthermore, the grain resistance is reflected by the left intercept at high frequency, and the resistance of the grain boundary is described by the diameter of the semicircle [29]. Plots of ionic conductivities were fitted with an equivalent circuit, as shown in Figure 5-6 (a). The R_s denote bulk resistance, the z denotes Warburg impedance, the parallel R_{ct}, and CPE_{dl} denotes the semicircle, and the second parallel RC circuit is employed for asymmetrical boundaries, impurity phases, and space charges [30]. All the synthesized samples' total conductivities, bulk, and grain boundary resistance values are shown in Table 5-2. The Mn-ternary composite sample exhibited the best electrochemical performance under ambient circumstances, with a total ionic conductivity of 2.22×10^{-4} Scm^{-1}. As explained by H. Yamada and H. Chung, one reason for this is lithium content agglomerating at grain boundaries and

grain surfaces, which may result in an increase in the number of charge carriers (Li^+) in the above two locations, changing the lithium deficient structure into a rich one [31,32]. The lower grain boundary resistance originating from the appropriate crystallinity and compact structure of the Mn-ternary composite pellet may also be significant for the enhanced electrochemical properties of the electrolyte synthesized at 900℃. At grain boundaries, the dense electrolyte may offer additional transfer paths for lithium-ion conduction.

Several studies have suggested that the growth of SiO_2 would be associated with the generation of amorphous silicate somewhere at the grain boundary, which might also bind the grains together and enhance the compaction density of solid electrolytes [33]. This phase may also let Li^+ ions move more easily from the grain core to the grain boundary phases, which would lead to an increase in the ionic conductivity of the grain boundaries. Furthermore, just becoming a non-lithium ionic conductor, the inordinate fraction of SiO_2 aggregates at the grain boundary and obstructs solid electrolyte ionic conduction [33]. It has been suggested that the inadequate densification of the electrolyte in the basic ternary composite and Co-ternary composite samples may be due to the formation of voids and cracks as a consequence of the rapid grain growth seen in these samples as a potential explanation for the increase in resistance reported for these samples.

Another possibility would be the formation of excessive impurity phases may serve as a barrier to the Li-ion conduction as described by T. Hupfer [34,35]. A compressed semicircle appears in the Co-ternary composite plot due to the roughness of the material, although it still exhibits the highest ionic conductivity values compared to the basic ternary composite sample. To achieve high ionic conductivity, a dense electrolyte structure in conjunction with a manganese dopant concentration has been used, which helps to limit inferior phase formation and promote the conduction of lithium ions at grain boundaries [6]. As shown in Table 5-3, there is the comparison of previously synthesized electrolytes with Mn-ternary composite ($AlPO_4$-SiO_2-$Li_4P_2O_7$) as a solid electrolyte for LIBs.

Table 5-2. R_s, $R_{ct,}$ and Ionic conductivities of ternary composite, Mn-ternary composite, and Co-ternary composite.

Samples ID	R_s (ohm)	R_{ct} (ohm)	Ionic Conductivity (S cm^{-1})
Ternary composite	1553	2.007×10^{6}	1.5214×10^{-5}
Mn-ternary composite	859	1.367×10^{5}	2.2214×10^{-4}
Co-ternary composite	2181	4.499×10^{5}	6.7594×10^{-5}

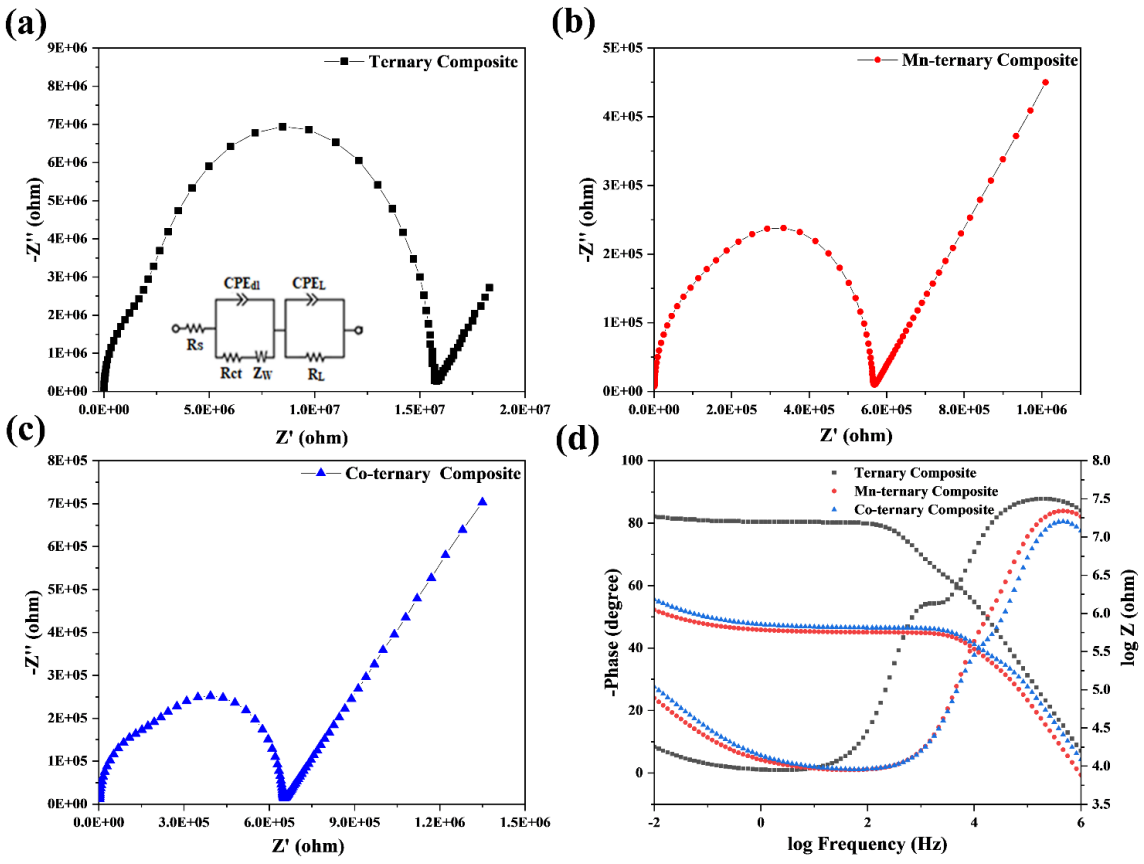

Figure 5-6. Nyquist plot of all solid electrolytes synthesized at 900 ^{o}C, (a) ternary composite, (b) Mn-ternary composite, (c) Co-ternary composite, and (d) Bode plot of ternary composite based SSEs for LIBs.

Figure 5-6 (d) illustrates the Bode plots of ternary composite, Co-ternary composite, and Mn-ternary composite sintered at 900 ℃. The conductivity graphs exhibit similar trends of conductivity to those seen in the Nyquist plot. Figure 5-7 depicts a comparison of the conductivities of the grain and the total ionic conductivities of each sample. The doping of manganese ions results in the formation of inferior phases such as $MnPO_4$, which segregates at grain boundaries and tends to bind the grains together, increasing the compact density. Although these phases agglomerate as the impurity concentration rises, they do not interfere with the conduction pathways of Li ions. High ionic conductivity may be achieved using a dense electrolyte structure with a significant concentration. This is accomplished by inhibiting excessive inferior phase formation and encouraging lithium-ion conduction at grain boundaries.

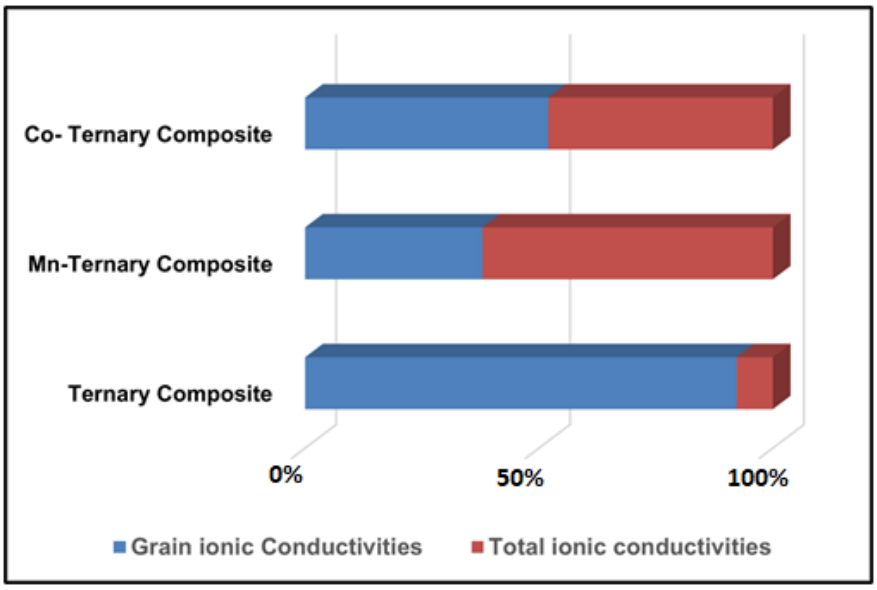

Figure 5-7. Comparing the grain and total ionic conductivities of ternary composite, Mn-ternary composite, and Co-ternary composite sintered at 900 °C.

Table 5-3. Comparison of previously synthesized electrolytes with Novel Oxide-based Mn-ternary composite ($AlPO_4$-SiO_2-$Li_4P_2O_7$) as a solid electrolyte for LIBs.

Sr No.	Solid State Electrolyte	Type of Electrolyte	Morphology	Ionic Conductivity (S cm^{-1})	Ref.
1	PEO/LiTFSI	Polymer based Electrolyte	Particle	3.7×10^{-5}	[36]
2	PAN/$LiClO_4$		Nanowires	6.05×10^{-5}	[37]
3	PMMA/$LiClO_4$		Particle	2.20×10^{-5}	[38]
4	$Mg_{0.5}ZrSn\ (PO_4)_3$	Oxide-based Electrolyte	Particle	2.47×10^{-5}	[39]
5	$Li_{1.5}Al_{0.5}Ti_{1.5}(PO_4)_3$		Particles	8×10^{-5}	[40]
6	Mn-ternary composite ($Li_4P_2O_7$-SiO_2-$AlPO_4$)	Ternary composite	Particle	2.21×10^{-4}	Present Work

Summary

All the results obtained during the research are discussed in this chapter. Characterization results of TGA, XRD, SEM, EDS, FTIR, Raman and EIS are supported with facts from previous studies and justified to understand the morphology, structure, composition, thermal stability, functional groups, surface area and porosity of the synthesized materials. Electrochemical results of the synthesized electrodes are discussed at the end. All the results are presented after comparison with the literature and are supported in the light of properties from characterization techniques.

References

[1] E. Antolini, "Lithium loss from lithium cobalt oxide: hexagonal Li0.5Co0.5O to cubic Li0.065Co0.935O phase transition," *Int. J. Inorg. Mater.*, vol. 3, no. 7, pp. 721–726, Nov. 2001, doi: 10.1016/S1466-6049(01)00185-4.

[2] B. Leo Brewer and J. Margrave, "Atomic Energy Commission Postdoctoral Fellow," *J. Am. Chem. Soc*, vol. 73, no. 2, p. 10, 1955, Accessed: Jun. 19, 2022. [Online]. Available: https://pubs.acs.org/sharingguidelines.

[3] H. Kimura, M. Asano, and K. Kubo, "Thermochemical study of the vaporization of Li2O(c) by mass spectrometric knudsen effusion method," *J. Nucl. Mater.*, vol. 92, no. 2–3, pp. 221–228, Sep. 1980, doi: 10.1016/0022-3115(80)90106-3.

[4] Y. Meesala *et al.*, "All-Solid-State Li-Ion Battery Using Li1.5Al0.5Ge1.5(PO4)3 As Electrolyte Without Polymer Interfacial Adhesion," *J. Phys. Chem. C*, vol. 122, no. 26, pp. 14383–14389, Jul. 2018, doi: 10.1021/ACS.JPCC.8B03971.

[5] Q. Wang, J. F. Wu, Z. Lu, F. Ciucci, W. K. Pang, and X. Guo, "A New Lithium-Ion Conductor LiTaSiO5: Theoretical Prediction, Materials Synthesis, and Ionic Conductivity," *Adv. Funct. Mater.*, vol. 29, no. 37, p. 1904232, Sep. 2019, doi: 10.1002/ADFM.201904232.

[6] F. Ma *et al.*, "Preparation and evaluation of high lithium ion conductivity Li1.3Al0.3Ti1.7(PO4)3 solid electrolyte obtained using a new solution method," *Solid State Ionics*, vol. 295, pp. 7–12, Nov. 2016, doi: 10.1016/J.SSI.2016.07.010.

[7] A. Manikandan *et al.*, "Rare earth element (REE) lanthanum doped zinc oxide (La: ZnO) nanomaterials: Synthesis structural optical and antibacterial studies," *J. Alloys Compd.*, vol. 723, pp. 1155–1161, Nov. 2017, doi: 10.1016/J.JALLCOM.2017.06.336.

[8] H. Rusdi, N. S. Mohamed, R. H. Y. Subban, and R. Rusdi, "Enhancement of electrical properties of NASICON-type solid electrolytes (LiSn2P3O12) via aluminium substitution," *J. Sci. Adv. Mater. Devices*, vol. 5, no. 3, pp. 368–377, Sep. 2020, doi: 10.1016/J.JSAMD.2020.06.003.

[9] R. O. Fuentes, F. M. Figueiredo, F. M. B. Marques, and J. I. Franco, "Influence of microstructure on the electrical properties of NASICON materials," *Solid State Ionics*, vol. 140, no. 1–2, pp. 173–179, Mar. 2001, doi: 10.1016/S0167-

2738(01)00701-9.

[10] A. Kumar and K. Shahi, “Particle size effect on ionic conductivity in NaCl□Al2O3 composite solid electrolytes,” *Solid State Commun.*, vol. 94, no. 9, pp. 813–816, Jun. 1995, doi: 10.1016/0038-1098(95)00063-1.

[11] G. Yan *et al.*, “Influence of sintering temperature on conductivity and mechanical behavior of the solid electrolyte LATP,” *Ceram. Int.*, vol. 45, no. 12, pp. 14697–14703, Aug. 2019, doi: 10.1016/J.CERAMINT.2019.04.191.

[12] S. Yu *et al.*, “Influence of microstructure and AlPO4 secondary-phase on the ionic conductivity of Li1.3Al0.3Ti1.7 (PO4)3 solid-state electrolyte,” *Funct. Mater. Lett.*, vol. 9, no. 5, Oct. 2016, doi: 10.1142/S1793604716500661.

[13] M. Illbeigi, A. Fazlali, M. Kazazi, and A. H. Mohammadi, “Effect of simultaneous addition of aluminum and chromium on the lithium ionic conductivity of LiGe2(PO4)3 NASICON-type glass–ceramics,” *Solid State Ionics*, vol. 289, pp. 180–187, Jun. 2016, doi: 10.1016/J.SSI.2016.03.012.

[14] D. M. Bykov, G. S. Shekhtman, A. I. Orlova, V. S. Kurazhkovskaya, E. Y. Borovikova, and V. Y. Volgutov, “Multivalent ionic conductivity in the series of phosphates LaxYb1/3 − xZr2(PO4)3 with NASICON structure,” *Solid State Ionics*, vol. 182, no. 1, pp. 47–52, Feb. 2011, doi: 10.1016/J.SSI.2010.11.019.

[15] C. R. Mariappan, G. Govindaraj, S. V. Rathan, and G. V. Prakash, “Preparation, characterization, ac conductivity and permittivity studies on vitreous M4AlCdP3O12 (M = Li, Na, K) system,” *Mater. Sci. Eng. B*, vol. 121, no. 1–2, pp. 2–8, Jul. 2005, doi: 10.1016/J.MSEB.2004.11.005.

[16] M. Junaid Bushiri, C. J. Antony, and A. Aatiq, “Raman and FTIR studies of the structural aspects of Nasicon-type crystals; AFeTi(PO4)3 [A=Ca, Cd],” *J. Phys. Chem. Solids*, vol. 69, no. 8, pp. 1985–1989, Aug. 2008, doi: 10.1016/J.JPCS.2008.02.008.

[17] W. Xia *et al.*, “Ionic Conductivity and Air Stability of Al-Doped Li7La3Zr2O12 Sintered in Alumina and Pt Crucibles,” *ACS Appl. Mater. Interfaces*, vol. 8, no. 8, pp. 5335–5342, Mar. 2016, doi: 10.1021/ACSAMI.5B12186/ASSET/IMAGES/AM-2015-121869_M002.GIF.

[18] O. Sheng *et al.*, “In Situ Construction of a LiF-Enriched Interface for Stable All-

Solid-State Batteries and its Origin Revealed by Cryo-TEM," *Adv. Mater.*, vol. 32, no. 34, p. 2000223, Aug. 2020, doi: 10.1002/ADMA.202000223.

[19] Y. Fu *et al.*, "A new insight into the LiTiOPO4 as an anode material for lithium ion batteries," *Electrochim. Acta*, vol. 185, pp. 211–217, Dec. 2015, doi: 10.1016/J.ELECTACTA.2015.10.124.

[20] R. Jiménez *et al.*, "Preparation and Characterization of Large Area Li-NASICON Electrolyte Thick Films," *Inorganics 2019, Vol. 7, Page 107*, vol. 7, no. 9, p. 107, Aug. 2019, doi: 10.3390/INORGANICS7090107.

[21] A. Das, P. S. R. Krishna, M. Goswami, and M. Krishnan, "Structural analysis of Al and Si substituted lithium germanium phosphate glass-ceramics using neutron and X-ray diffraction," *J. Solid State Chem.*, vol. 271, pp. 74–80, Mar. 2019, doi: 10.1016/J.JSSC.2018.12.038.

[22] K. Arbi, M. Hoelzel, A. Kuhn, F. García-Alvarado, and J. Sanz, "Structural factors that enhance lithium mobility in fast-ion Li 1+xTi2-xAlx(PO4)3 ($0 \leq x \leq 0.4$) conductors investigated by neutron diffraction in the temperature range 100-500 K," *Inorg. Chem.*, vol. 52, no. 16, pp. 9290–9296, Aug. 2013, doi: 10.1021/IC400577V/SUPPL_FILE/IC400577V_SI_001.PDF.

[23] D. Petit, P. Colomban, G. Collin, and J. P. Boilot, "Fast ion transport in LiZr2(PO4)3: Structure and conductivity," *Mater. Res. Bull.*, vol. 21, no. 3, pp. 365–371, Mar. 1986, doi: 10.1016/0025-5408(86)90194-7.

[24] T. Gao, H. Fjellvåg, and P. Norby, "A comparison study on Raman scattering properties of α- and β-MnO2," *Anal. Chim. Acta*, vol. 648, no. 2, pp. 235–239, 2009, doi: 10.1016/j.aca.2009.06.059.

[25] A. V. Ravindra, B. C. Behera, and P. Padhan, "Laser induced structural phase transformation of cobalt oxides nanostructures," *J. Nanosci. Nanotechnol.*, vol. 14, no. 7, pp. 5591–5595, 2014, doi: 10.1166/jnn.2014.9023.

[26] M. Barj, G. Lucazeau, and C. Delmas, "Raman and infrared spectra of some chromium Nasicon-type materials: Short-range disorder characterization," *J. Solid State Chem.*, vol. 100, no. 1, pp. 141–150, Sep. 1992, doi: 10.1016/0022-4596(92)90164-Q.

[27] M. Barj, H. Perthuis, and P. Colomban, "Relations between sublattice disorder,

phase transitions and conductivity in NASICON," *Solid State Ionics*, vol. 9–10, no. PART 2, pp. 845–850, Dec. 1983, doi: 10.1016/0167-2738(83)90100-5.

[28] P. Tarte, A. Rulmont, and C. Merckaert-Ansay, "Vibrational spectrum of nasicon-like, rhombohedral orthophosphates MIMIV2(PO4)3," *Spectrochim. Acta Part A Mol. Spectrosc.*, vol. 42, no. 9, pp. 1009–1016, Jan. 1986, doi: 10.1016/0584-8539(86)80012-5.

[29] H. S. Jadhav *et al.*, "Influence of B2O3 addition on the ionic conductivity of Li1.5Al0.5Ge1.5(PO4)3 glass ceramics," *J. Power Sources*, vol. 241, pp. 502–508, Nov. 2013, doi: 10.1016/J.JPOWSOUR.2013.04.137.

[30] M. Y. Hassaan, S. M. Salem, and M. G. Moustafa, "Study of nanostructure and ionic conductivity of Li1.3Nb0.3 V1.7(PO4)3 glass ceramics used as cathode material for solid batteries," *J. Non. Cryst. Solids*, vol. 391, pp. 6–11, May 2014, doi: 10.1016/J.JNONCRYSOL.2014.03.001.

[31] H. Chung and B. Kang, "Increase in grain boundary ionic conductivity of Li1.5Al0.5Ge1.5(PO4)3 by adding excess lithium," *Solid State Ionics*, vol. 263, pp. 125–130, Oct. 2014, doi: 10.1016/J.SSI.2014.05.016.

[32] H. Yamada, D. Tsunoe, S. Shiraishi, and G. Isomichi, "Reduced grain boundary resistance by surface modification," *J. Phys. Chem. C*, vol. 119, no. 10, pp. 5412–5419, Mar. 2015, doi: 10.1021/JP510077Z/SUPPL_FILE/JP510077Z_SI_001.PDF.

[33] Z. Kou, C. Miao, Z. Wang, and W. Xiao, "Novel NASICON-type structural Li1.3Al0.3Ti1.7SixP5(3-0.8x)O12 solid electrolytes with improved ionic conductivity for lithium ion batteries," *Solid State Ionics*, vol. 343, p. 115090, Dec. 2019, doi: 10.1016/J.SSI.2019.115090.

[34] T. Hupfer *et al.*, "Evolution of microstructure and its relation to ionic conductivity in Li1 + xAlxTi2 − x(PO4)3," *Solid State Ionics*, vol. 288, pp. 235–239, May 2016, doi: 10.1016/J.SSI.2016.01.036.

[35] C. M. Chang, S. H. Hong, and H. M. Park, "Spark plasma sintering of Al substituted LiHf2(PO4)3 solid electrolytes," *Solid State Ionics*, vol. 176, no. 35–36, pp. 2583–2587, Nov. 2005, doi: 10.1016/J.SSI.2005.07.010.

[36] L. Han *et al.*, "Flame-Retardant ADP/PEO Solid Polymer Electrolyte for Dendrite-

Free and Long-Life Lithium Battery by Generating Al, P-rich SEI Layer," *Nano Lett.*, vol. 21, no. 10, p. 59, May 2021, doi: 10.1021/ACS.NANOLETT.1C01137/ASSET/IMAGES/LARGE/NL1C01137_0005.JPEG.

[37] W. Liu *et al.*, "Enhancing ionic conductivity in composite polymer electrolytes with well-aligned ceramic nanowires," *Nat. Energy 2017 25*, vol. 2, no. 5, pp. 1–7, Apr. 2017, doi: 10.1038/nenergy.2017.35.

[38] J. Sun, Y. Li, Q. Zhang, C. Hou, Q. Shi, and H. Wang, "A highly ionic conductive poly(methyl methacrylate) composite electrolyte with garnet-typed Li6.75La3Zr1.75Nb0.25O12 nanowires," *Chem. Eng. J.*, vol. 375, p. 121922, Nov. 2019, doi: 10.1016/J.CEJ.2019.121922.

[39] M. Mustafa, M. S. A. Rani, S. B. R. S. Adnan, F. M. Salleh, and N. S. Mohamed, "Characteristics of new Mg0.5(Zr1-xSnx)2(PO4)3 NASICON structured compound as solid electrolytes," *Ceram. Int.*, vol. 46, no. 18, pp. 28145–28155, Dec. 2020, doi: 10.1016/J.CERAMINT.2020.07.313.

[40] Z. Cai, Y. Huang, W. Zhu, and R. Xiao, "Increase in ionic conductivity of NASICON-type solid electrolyte Li1.5Al0.5Ti1.5(PO4)3 by Nb2O5 doping," *Solid State Ionics*, vol. 354, p. 115399, Oct. 2020, doi: 10.1016/J.SSI.2020.115399.

Chapter 6: Conclusions and Recommendations

6.1 Conclusions

A novel oxide-based ternary composite ($AlPO_4$-SiO_2-$Li_4P_2O_7$) solid-state electrolyte for lithium batteries was successfully synthesized using a conventional solid-state technique. Manganese and cobalt were doped and substituted into the lattice structure of ternary composites, as indicated by XRD spectra. When Mn and Co were incorporated into the ternary composite, the peaks of AlPO4, $Li_2P_4O_7$, and SiO_2 became variated in their intensities, as determined by XRD, FTIR, and Raman studies. The Mn-ternary composite seems to have a compact density and average particle size of 1.55 µm and few pores and cracks within the electrolyte, as confirmed by SEM analysis. In contrast to other specimens, the Mn-ternary composite sample exhibited a higher ionic conductivity of 2.21×10^{-4} S cm^{-1}. The ionic conductivity was demonstrated to be directly related to the microstructure and morphology of the electrolyte. Various synthesis techniques, including the Sol-gel method, melt quenching, and microwave-assisted sintering, may also be utilized to modify the microstructure and morphology of the material to boost the ionic conductivity of an electrolyte. The findings of the Mn-ternary composite show that it is cost-effective and has the potential to be employed as a solid-state electrolyte in the realm of lithium batteries in the coming years.

6.2 Recommendations

The electrochemical performance and efficiency of ASSLBs can be increased by exploring new combinations of materials to be employed as electrolytes, in addition to the informed selection of electrode materials. The following recommendations are presented to address the shortcomings in the research regarding the solid electrolyte materials:

- Focus of the future research should be towards the various tetravalent cations and a hybrid oxide and sulfide-based structure to offer stability and high electrochemical performance for ASSLBs.
- Ceramics and polymer composites should be explored to enhance the stretch, flexibility, and ionic conductivities of the electrolytes.

- In contrast to traditional Li-ion batteries, ASSLBs lack the required power density. Therefore, research is required in the direction of sodium ion batteries to ensure maximum power density and energy density simultaneously.

Appendix 1 – Publications

Tailoring the Electrochemical Properties of Novel Oxide-Based Ternary Composite ($AlPO_4$-SiO_2- $Li_4P_2O_7$) Solid-State Electrolyte for Lithium Batteries

Hafiz Muhammad Haseeb,[a] Altamash Shabbir,[a] Zuhair S. Khan,[a] Ghulam Ali[a,*]

[a]U.S.-Pakistan Center for Advanced Studies in Energy, National University of Sciences and Technology (NUST), Islamabad, 44000, Pakistan

Abstract

One of the most electrifying and interesting supporting components for the advancement of next-generation lithium batteries is a solid-state electrolyte. Oxide-based solid electrolytes are gaining popularity among researchers owing to their great stability, although they have inadequate ionic conductivity due to high grain boundary resistance. In this work, a novel oxide-based ternary composite ($AlPO_4$-SiO_2-$Li_4P_2O_7$) electrolyte is synthesized via a conventional solid-state process with excellent water stability and high ionic conductivity. The crystallographic structure of ternary composite is confirmed using X-ray diffraction and has a significant effect on ionic conductivity. The thermogravimetric analysis result shows a 22.26 wt.% loss in the region of 25 °C to 900 °C due to the degradation of volatile constituents including nitrates, chlorides, and water. BET results revealed that the material is compact and dense and having low porosity and surface area. The morphological assessment is carried out using scanning electron microscopy to observe the growth of grains. The Raman and Fourier transformed infra-red spectroscopies are used to scrutinize the structural and functional group analysis of the solid-state electrolyte. Electrochemical impedance spectroscopy is used to evaluate ionic conductivities. The ternary composite sintered at 900 °C has shown ionic conductivity of 2.21×10^{-4} S cm^{-1} at ambient temperature. These findings suggest that a solid electrolyte composed of ternary composites could be a credible candidate for lithium batteries.

Keywords: Lithium batteries; solid-state electrolyte; ternary composite; dopants; ionic conductivity.

Journal: **Physica B: Physics of Condensed Matter**

Status: **Under Review**